LAWRENCE
LIVERMORE
NATIONAL
LABORATORY

LLNL-JRNL-651172

An in-flight radiography platform to measure hydrodynamic instability growth in inertial confinement fusion capsules at the National Ignition Facility

V. A. Smalyuk, D. T. Casey, S. W. Haan, D. E. Hoover, O. A. Hurricane, J. J. Kroll, A. Nikroo, J. L. Peterson, B. A. Remington, H. F. Robey, D. S. Clark, B. A. Hammel, O. L. Landen, M. Marinak, D. H. Munro, K. J. Peterson, J. Salmonson

March 4, 2014

Physics of Plasmas

Disclaimer

An in-flight radiography platform to measure hydrodynamic instability growth in inertial confinement fusion capsules at the National Ignition Facility.

K. S. Raman[1], V. A. Smalyuk[1], D. T. Casey[1], S. W. Haan[1], D. E. Hoover[3], O. A. Hurricane[1], J. J. Kroll[1], A. Nikroo[3], J. L. Peterson[1], B. A. Remington[1], H. F. Robey[1], D. S. Clark[1], B. A. Hammel[1], O. L. Landen[1], M. Marinak[1], D. H. Munro[1], K. J. Peterson[2], J. Salmonson[1]
[1]*Lawrence Livermore National Laboratory, Livermore, CA 94550*
[2]*Sandia National Laboratory, Albuquerque, NM 87125 and*
[3]*General Atomics, San Diego, CA 92121*
(Dated: July 9, 2014)

A new in–flight radiography platform has been established at the National Ignition Facility (NIF) to measure Rayleigh–Taylor (RT) and Richtmyer–Meshkov (RM) instability growth in inertial confinement fusion (ICF) capsules. The platform has been tested up to a convergence ratio of 4. An experimental campaign is underway to measure the growth of pre–imposed sinusoidal modulations of the capsule surface, as a function of wavelength for a pair of ignition–relevant laser drives: a "low–foot" drive representative of what was fielded during the National Ignition Campaign (NIC) [1] and the new high–foot [2, 3] pulse shape, for which the predicted instability growth is much lower. We present measurements of Legendre modes 30, 60, and 90 for the NIC–type, low–foot, drive and modes 60 and 90 for the high–foot drive. The measured growth is consistent with model predictions, including much less growth for the high–foot drive, demonstrating the instability mitigation aspect of this new pulse shape. We present the design of the platform in detail and discuss the implications of the data it generates for the on–going ignition effort at NIF.

I. INTRODUCTION

We present a new experimental platform for measuring Rayleigh–Taylor (RT) [4–6] and Richtmyer–Meshkov (RM) [7–9] instability growth in inertial confinement fusion (ICF) [10–12] capsules at the National Ignition Facility (NIF) [13]. These hydrodynamic instabilities can significantly lower ICF capsule performance by degrading the ablator's ability to compress the fusion fuel and/or by mixing ablator material into the fusion fuel [10–12]. Our work was motivated by observations of high levels of fuel–ablator mixing in many of the implosions studied during the National Ignition Campaign (NIC) [14–16]. One purpose of our experiments is to compare direct measurements of ICF capsule RT/RM growth with the simulations used to predict the growth before NIC [17], as part of the effort to understand why the NIC capsules failed to approach ignition conditions as ignition–relevant implosion velocities were reached [1].

The source of the discrepancy between expectations and reality is not fully understood. 2D simulations can be tuned to match much of the NIC performance data by artificially multiplying the measured capsule surface roughness by factors of 3–5 and/or by artificially pre–mixing ablator material into the fusion fuel [18]. Taken literally, this implies a level of instability growth much larger than simulated, or an initial condition seeding the growth much larger than currently understood from the capsule surfaces, or some other internal structure. However, 3D simulations [19], and recent measurements indicating the importance of low–mode asymmetries [20], the capsule support tent [21], and hot electron preheat [22], suggest the poor performance of the NIC implosions could be a combined effect of mix and several other non–ideal features. Therefore, both the refinement of instability models and the mitigation of instability effects are expected to be important aspects of ignition design moving forward. The NIC instability models have been validated at lower energy densities through Nova laser experiments involving x–ray driven planar foils with pre-imposed single and multimode perturbations [23–28] and similar experiments in converging geometries [29, 30]. Our experiment was developed both to extend this validation status into the high energy density regime relevant for ignition and to provide a platform for evaluating the effectiveness of mitigation strategies.

The experimental geometry (Fig. 1) involves a plastic capsule, with a sinusoidal ripple machined on its outer surface, mounted on the tip of a cone in a gold, keyhole–type hohlraum [31]. 184 of the 192 NIF laser beams are focused on the hohlraum walls generating soft x–rays which drive the capsule, with peak drive corresponding to radiation temperatures around 300 eV . The remaining 8 beams are focused on a 12.5 μm thick vanadium foil outside the hohlraum to generate 5.4 keV backlighter x–rays which radiograph the capsule in–flight. The backlighter x–rays enter the hohlraum through the cone; pass through the rippled capsule surface; and exit the hohlraum through a window towards a gated x–ray camera [32].

As the capsule implodes on the cone, the perturbation develops from a sinusoidal ripple into a spike–bubble pattern (Fig. 2ab). Simulations predict the ripple increases in amplitude while the density also changes due to compression/decompression and convergence [33, 34], and becomes more modulated due to mass moving from bubbles to spikes. These effects determine the optical depth experienced by a backlighter x–ray:

$$OD \equiv \int \kappa \rho dl \tag{1}$$

where κ is the opacity, ρ the density, and the integral is along the path of the x–ray. An x–ray passing through a spike will experience a larger OD, hence greater absorption, than a neighboring x–ray passing through a bubble, resulting in a

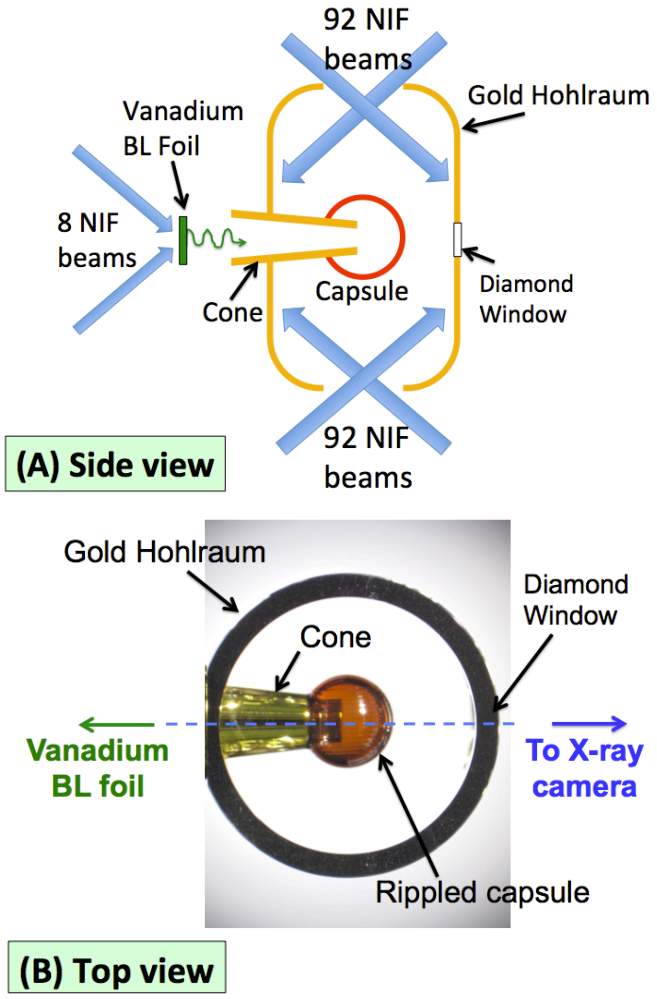

FIG. 1: Experiment geometry, side (not–to–scale) and top views.

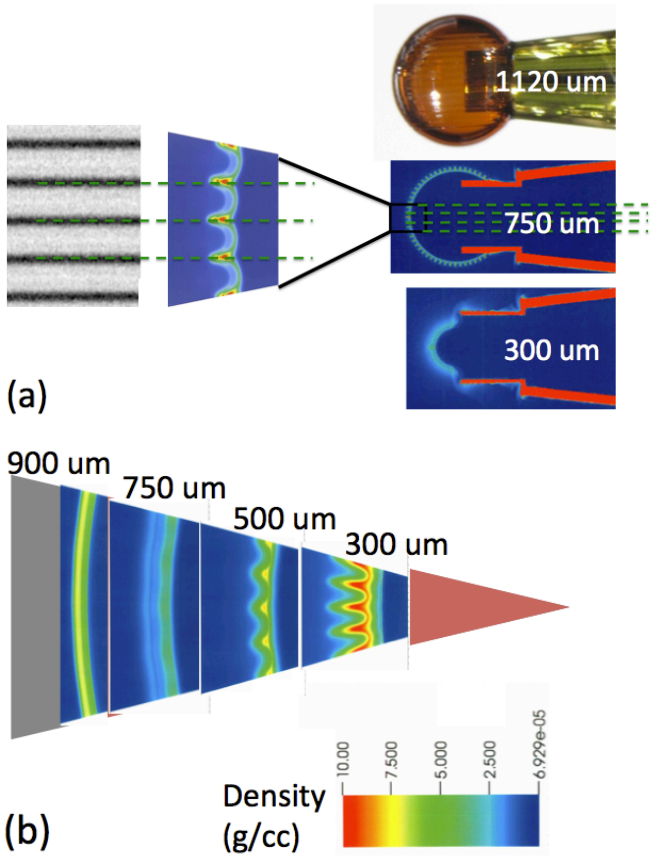

FIG. 2: (a) In a face–on radiograph, the contrast relates directly to perturbation growth. The figure shows a synthetic radiograph at 750 μm capsule radius, the dashed lines depicting x–rays. The simulation frame at 300 μm capsule radius suggests the technique remains viable even when the capsule is smaller than the $\sim$ 800 μm cone opening. (b) During an implosion, in addition to amplitude growth, the density also changes and becomes modulated.

striped radiographic image for the 2D perturbations considered here (Fig. 2). The modulation in optical depth is the key quantity measured by this face–on radiography technique and relates directly to the perturbation growth. The x–ray camera is gated to capture four images per experiment, and Fig. 3 is an example of the data obtained in a typical shot.

Our platform is designed to use the same laser drives, capsules, and hohlraums as ignition experiments on NIF [35], modulo the absence of a cryogenic deuterium–tritium (DT) ice layer, in order to study instability growth under nominally identical conditions. Measurements are taken at convergence ratios (CR) of 1.2 to 4, corresponding to the acceleration phase of the implosion, where we define the convergence ratio as the ratio of the initial capsule outer radius ($\sim$ 1 mm) to the ablation front radius at measurement time. The $CR \sim 1.2$ limit corresponds to the beginning of peak laser power (see Fig. 4) and is about when the seeded perturbations first reach a diagnosable size. The $CR \sim 4$ limit is approaching the time when peak capsule velocity is reached in a typical implosion; beyond this point, an ignition capsule will decelerate due to the back pressure from the fuel vapor inside. Our capsules (and cone) are vacuum–filled, so the deceleration phase is not accessible to this platform, as currently designed. However, if surrogacy with ignition experiments is not required, simulations indicate the platform remains viable at convergence ratios higher than this [36].

A different type of surrogacy is with regard to the instability growth itself. In order for the growth to be observable, we require the machined ripples to have much higher initial amplitudes than what is present in an ignition capsule surface finish [17] at the same wavelengths. However, the initial amplitudes are designed to be small enough that the (predicted) growth remains close to linear during the measurement window, in the sense of the final amplitude being proportional to the initial amplitude. Therefore, we expect the growth factors, i. e. the ratios of final to initial amplitudes, measured in this platform to be reasonably close to the growth factors (of the much smaller perturbations) in actual ICF targets.

Our main result is that this new in–flight radiography capability is now established [37] and is being used to investigate a variety of topics that directly impact ICF capsule performance. An experimental campaign is underway to measure

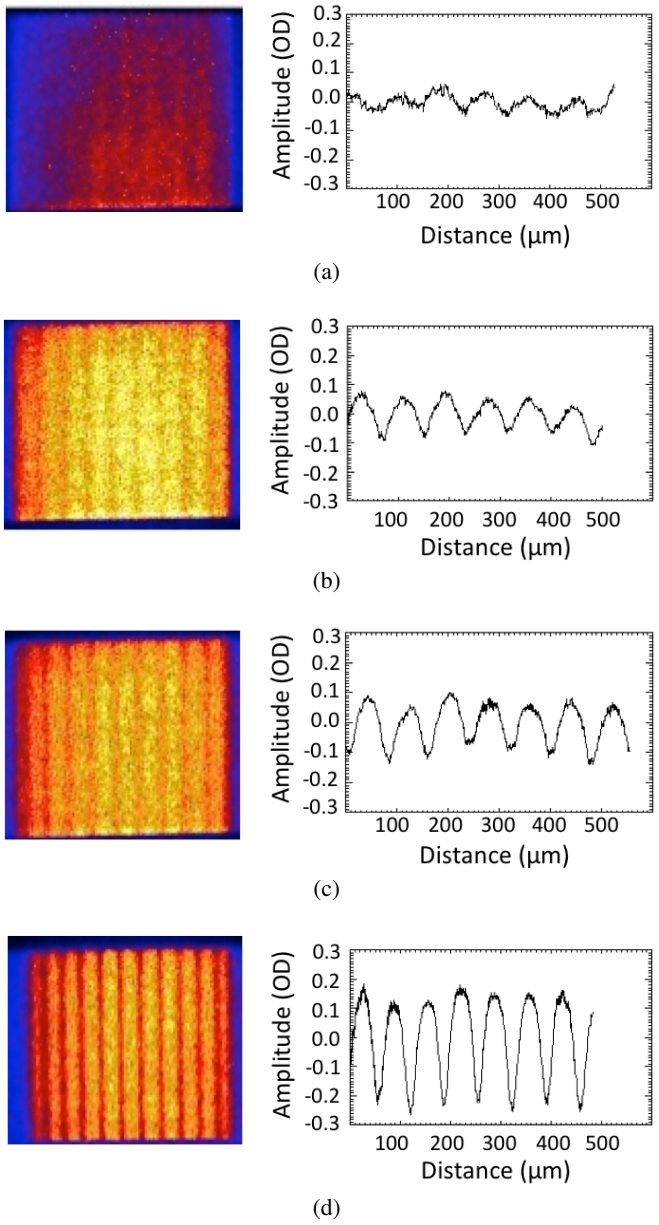

FIG. 3: Data for shot N130702: mode 60, 1.7 μm initial amplitude, high–foot drive. Slit images are obtained at four times during the implosion: (a) t=12.8 ns, $CR = 1.3$, (b) t=13.3 ns, $CR = 1.4$, (c) t=13.7 ns, $CR = 1.5$, (d) t=14.4 ns, $CR = 1.75$. The line spacing in the images becomes narrower with time due to convergence. In frame (d), the effect of the radiograph being a planar projection of a curved capsule surface is seen in the line spacing becoming narrower towards the edge of the field–of–view. The lineouts are of the optical depth, averaged over the slit dimension, of a central section of the images, where the zero point is referenced to the average transmission, and the backlighter profile has been subtracted. The lineouts show the evolution of the perturbation from a sinusoidal modulation to a weakly nonlinear spike–bubble pattern.

the instability growth versus Legendre mode number for a pair of ignition–relevant laser drives (Fig. 4): a high–gain ignition design [17, 38] representative of what was fielded during NIC, which we refer to as the "low–foot" pulse, and the more recent "high–foot" pulse [2, 3, 39], which trades one–dimensional ignition margin for additional margin in a number of respects, including much lower instability growth. In addition to discussing the platform design in detail, we compare post–shot simulations with data up to $CR \sim 2$ for modes 30, 60, and 90 for the low–foot pulse [40], and modes 60 and 90 for the high–foot pulse [41]. For both drives, the measurements agree fairly well with post–shot models, providing the first validation of the NIC instability models, and in particular the capsule–only modeling framework presented in Ref. 18, in the ignition–relevant regime. Much lower instability growth is measured for the high–foot drive, demonstrating the instability mitigation aspect of the new pulse shape. The platform itself has been successfully tested at $CR = 4$ and measurements at higher mode numbers (120 and 160) are underway; these will be discussed in a separate publication. Future experiments are being planned to investigate 3D surface roughness [42], features such as the support tent [21, 43, 44], the sensitivity of RT/RM growth to alternate ablators and pulse shape variations [45], and more.

What is novel about our experiments is that these are the first measurements of acceleration phase instability growth in a physical regime and experimental geometry directly applicable to the indirect–drive ignition effort at NIF. Face–on radiography instability measurements in spherical ICF implosions at lower energy densities have been done for indirectly–driven targets on the Nova laser [29, 30] and Z–facility [46], and for directly–driven targets on the Omega laser [47]. Side–on radiography has been used in a similar way to quantify instability growth in cylindrical implosions for directly–driven [48, 49], indirectly–driven [50], and magnetically–driven [51–55] systems. There has also been ICF–relevant work done in planar geometries, exploring basic aspects of ablative stabilization [23–28, 56–64] and the laser imprint issue relevant for direct–drive [59, 65–70]. While our work was motivated largely by its application to ICF, there is a larger body of work exploring hydrodynamic instabilities from the standpoint of astrophysics or basic high energy density science, that is beyond the scope of this present article, but discussed, for example, in Refs. 71, 72.

In section II, we discuss the models and simulations. In section III, we discuss the platform design. In section IV, we compare the data from the on–going experimental campaign with post–shot simulations. In section V, we discuss how this platform can be used to refine models, as well as potential issues with data interpretation. We conclude with a summary.

II. MODELS

All of the design simulations in this paper are performed with the HYDRA code [73], except for the simulations of the capsule on the cone (Fig. 2a), which use the ARES code [74], both codes developed at Lawrence Livermore National Laboratory. These codes use arbitrary Lagrangian–Eulerian (ALE) methods for the hydrodynamic mesh motion and advection.

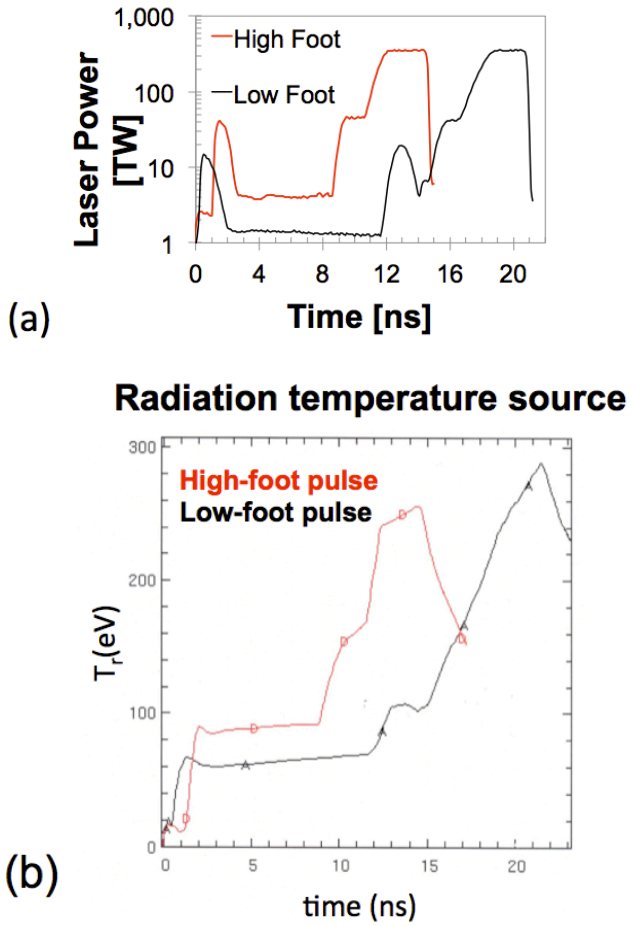

FIG. 4: The experiments in this paper use (a) the low–foot and high–foot pulse shapes. (b) We model these pulse shapes as effective radiation temperature sources, calibrated to match measured implosion data for the two pulse shapes via the procedure outlined in Section II.

The simulations include multigroup radiation diffusion, electron heat conduction, tabulated equations of state and opacities, and a Thomas–Fermi type model for ionization. Model settings, such as ALE strategies, time step controls, radiation group bin structure, etc., closely follow what was used for capsule–only modeling studies during NIC, as described, for example, in Ref. 18, since our platform is designed to validate that framework. For simulations of capsules with pre–imposed sinusoidal ripples, the mesh resolution is 64 angular zones per wavelength with radial zoning that slowly feathers from a 100 nm zone thickness at the outer capsule surface, in order to resolve the early time development of the ablation front, to a uniform spacing of about 600 nm within the ablator.

Capsule–only models simulate the ICF capsule while treating the hohlraum environment implicitly as a frequency–dependent radiation source applied to zones on the problem boundary. This enables the study of capsule–focused issues, such as instability growth, which requires much higher resolution than what is currently feasible for integrated simulations that explicitly model the hohlraum and laser [75]. An important technical step in this approach is constructing a radiation source that accurately represents the action of the laser pulse on the capsule. Integrated hohlraum simulations do not predict measured implosion features, which are highly sensitive to complex details of laser–plasma interactions [76, 77] and warm dense material properties [12], accurately enough for us to use these directly as sources for the hydrodynamic instability simulations.

Therefore, the current method of constructing capsule radiation sources involves an initial source from a hohlraum simulation, which is then further tuned to match implosion data for the specific laser pulse, following the procedure described in Ref. 18. The standard calibration data include shock velocities from VISAR measurements [31, 78], the ablator trajectory and remaining mass from convergent ablator (conA) experiments [79]; and the bang time from experiments with a neutron yield. The tuning is accomplished though multipliers on the total radiation flux as well as adjustments to the relative brightness of the "M–band" part of the spectrum, defined as energies $h\nu > 1.8$ keV. In addition to matching the above data, we adjust the M–band content in our sources to be consistent with data from the new viewfactor platform [80], which directly measures the radiation field seen by the capsule. As emphasized in Ref. 18, the tuned radiation source is *not* intended to be an accurate representation of the radiation field seen by the capsule, but is interpreted simply as an effective drive that reproduces the measured implosion features. In this approach, the source multipliers are a means of accounting for missing physics, including physics uncertainties unrelated to the radiation field that could have been accounted for in other ways, for example by adjusting the equation–of–state or opacity tables.

We select laser pulses previously used in ignition experiments, both to leverage the availability of the data to create these calibrated sources and so our experiment could be used to validate the procedure. Fig. 4b shows the radiation temperature versus time of the data–calibrated sources for our two pulse shapes. While strongly constrained by the data, there is still uncertainty in our calibrated sources, both due to measurement uncertainties in the calibration data and sensitivity to modeling inputs such as the equation–of–state and opacity tables. In the comparisons with experimental data presented below, we also discuss the uncertainty in our simulated results, which is dominated by this residual uncertainty in the frequency–dependent radiation sources.

We compare the data with simulations in two different ways. The first way, as done in Figures 15 to 19, directly compares the measurements with simulations of the actual experimental conditions, given in Table I. We model the as–shot dimensions of the capsule and perturbations. We account for the (usually small) differences between the requested and delivered laser pulse by adjusting the frequency–dependent radiation source using the following prescription, appropriate for deviations of order $\sim 10\%$, based on simulation studies that investigated this issue: the source radiation flux adjustment is approximately twice the laser power deviation in the "picket" of the pulse and proportional to the power deviation

for the rest of the pulse, for both the high–foot and low–foot pulses [81]. We model the effect of the 8 missing backlighter beams, in shots where they were not explicitly compensated for in the experiment by making power adjustments to the remaining beams (see Table I), as an additional $\sim 4\%$ (8/192) laser power reduction applied for the duration of the pulse. The present models do not include the radiation drive asymmetry or non–ideal aspects of the capsule, such as the surface roughness or manufacturing defects, as we expect both of these to be very small effects at the convergence ratios when we take data, i. e. up to $CR = 2$. In section V, we will discuss the validity of these various modeling approximations.

The second type of comparison, done in Figure 20, is in terms of the linear growth factor dispersion curve. The growth factor of a mode is the ratio of the final amplitude of the perturbation to its initial amplitude. In the linear regime, the growth factor versus mode number is independent of the amplitude and spectrum of the initial condition, which makes it a useful quantity for characterizing the instability properties of ICF designs. For amplitudes typical of ICF capsule surfaces, models predict linear growth up to $CR = 2$, discussed more in section III C, and possibly for the entire acceleration [17]. Therefore, if the machined perturbations remain close to linear, a growth factor curve measured in this experiment will provide a reasonable estimate of the "real" growth factor curve of an ICF target. The tradeoff between having large perturbations for diagnosability versus smaller amplitudes to ensure linearity is discussed more in section III C.

The curves in Fig. 20 are simulations of the linear optical depth growth factor for different radiation sources, where the ratio is between the final and initial values of the amplitude of the optical depth modulation, labeled "amplitude (OD)", defined as the first harmonic of the radiograph lineout over a suitably chosen analysis region. The curves are obtained by post–processing a series of single mode simulations where the initial amplitude is small enough (50 nm) that the predicted growth is linear up to $CR = 2$. The data are experimentally–based estimates of the "real" growth factor curve, which involves applying a correction factor to the measurements to account for our best estimate of the effect of nonlinear saturation [6, 82, 83] on the growth rate; the correction factor is discussed more below and in Appendix B.

We calculate the initial amplitude reference for both the simulated curves and experimental data placed on these plots explicitly. The initial amplitude (OD) is given by $(\kappa\rho)a_0$ where a_0 is the initial amplitude of the surface perturbation and $1/(\kappa\rho)$ is the attenuation length at the backlighter energy in the undoped plastic, which is where the perturbation initially lies. For a 5.4 keV backlighter energy and undoped glow discharge polymer (GDP) plastic ($C_{0.423}H_{0.572}O_{0.005}$), the attenuation length is $1/(\kappa\rho) = 690\mu$m [84].

III. PLATFORM DESIGN

Our platform is designed to accommodate a scenario where the models differ significantly from reality in this new ignition–relevant regime. Therefore, much of the design is based on having an optimal measurement and mitigating possible failure modes, in order to maximize the (probability of) data return within a very limited shot allocation. These design aspects are described in this section.

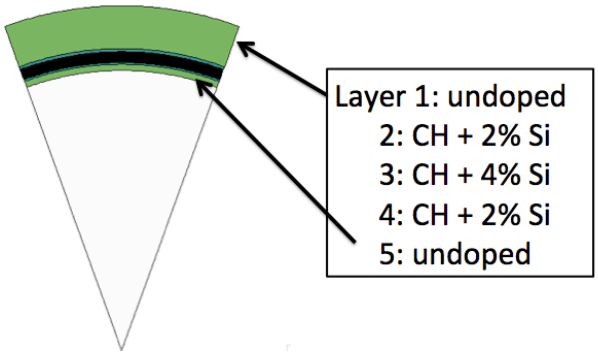

FIG. 5: The experiments in this paper use standard 2xSi symmetry capsules.

A. Capsule

The experiment uses the same ~ 2 mm diameter, silicon–doped GDP plastic capsules (Fig. 5) as ignition targets, except the plastic shells are thicker (~ 210 μm vs. ~ 195 μm) with an extra 15 μm of plastic in place of the cryogenic fuel layer to obtain the same mass [85]. The dopant is added in a five–layer profile, matching the configuration used in ignition targets: the innermost and outer layers are undoped, while the interior layers have atomic concentrations of 2%, 4%, and 2% silicon respectively. We use this "2xSi" profile over the more commonly used 1xSi profile (where the interior layers have 1%, 2%, and 1% dopant) primarily to enhance the radiographic contrast while qualifying the platform, though simulations indicate the growth also changes. The 2xSi profile was used in a number of ignition experiments during NIC, including the N120321 shot which achieved the highest fuel compression to date [38] and on which our low–foot pulse shape is based.

Fig. 6 shows how the density and optical depth vary for a 2xSi capsule driven with a low–foot pulse. An optimal backlighter has an average optical depth between 1 and 2 so that optically thinner and thicker regions appear clearly as lighter and darker parts of the radiograph. Because the capsule density rapidly increases in the working range of the experiment, the optimal backlighter also changes. We use vanadium ($\sim$5.4 keV), which is optimal around peak acceleration, $CR \sim 2$. Scandium (4.3 keV) is ideal for the early acceleration stage while iron (6.7 keV) is needed at $CR \sim 4$. The optical depth which enters the optimization includes not only the optical depth of the capsule shown in Fig. 6, but also accounts for absorption in the diagnostic windows and filters [40].

The spectral content of the x–rays used in the imaging system is measured using the absorption of a 30 μm thick aluminum strip placed in front of the framing camera on each

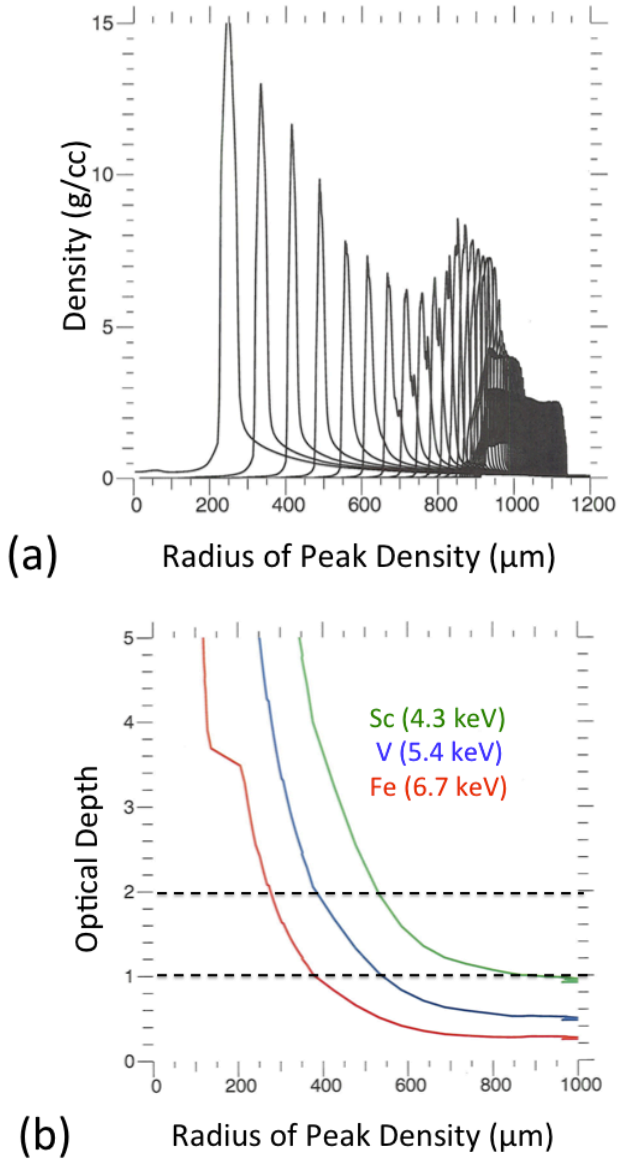

FIG. 6: (a) Density and (b) optical depth for various backlighters as a function of implosion radius for a 2xSi capsule, driven by a low–foot drive. An optimal backlighter will have optical depth between 1 and 2.

shot. In each shot the measured strip attenuation is consistent with 5.4 keV x–rays generated by the K–shell of the vanadium backlighter.

B. Hohlraum

The experiment uses a standard gold hohlraum, 9.43 mm in length and 5.75 mm inner diameter, with 3.1 mm diameter entrance holes for the laser beams at both ends. The hohlraum is filled with helium gas, with density 0.96 mg/cc (low–foot) or 1.6 mg/cc (high–foot), to tamp the gold plasma blowoff that interferes with the beam propagation [86]. The capsule is mounted on the tip of a gold cone extending from just outside the hohlraum wall to just inside the capsule interior. The arrangement resembles the NIF shock timing platform [31], with a few differences. First, since our experiment studies the acceleration stage, the cone is truncated to not interfere with the capsule motion. Second, our capsule is vacuum–filled, while the shock–timing capsule–cone is typically filled with liquid deuterium [87]. Third, there is a diamond diagnostic window opposite the cone, providing a 250 μm by 900 μm field–of–view for the x–ray imaging camera. This radiography line–of–sight is similar to the NIF convergent ablator (conA) platform [79], except the backlighter x–rays now pass through the cone and a single capsule surface, instead of entering through an additional window and passing through two capsule surfaces. This experiment is the first time this single pass radiography technique, which enables much higher quality data, has ever been fielded.

A key concern is gold entering the radiography line–of–sight, as even a small density of gold would absorb the backlighter x–rays and effectively end the experiment. The ways this could happen relate to how our experiment places additional strain on design elements incorporated from the successful VISAR and conA platforms. For instance, we use a thinner diagnostic window (80 μm vs. 130 μm) than conA experiments to ensure adequate transmission of our softer backlighter (5 keV vs. 9 keV). While a thinner window implies greater transmission, it also increases the chance of the window closing during the experiment. Simulations shown in Fig. 7 indicate that an 80 μm thick window is sufficient to keep the line of sight open.

Two more failure modes, illustrated in Fig. 8, relate to the cone and our experiment running much later in time than keyhole shock timing experiments, and without the liquid deuterium fill which would effectively tamp away these effects. First, our cone is thicker than what is normally used in VISAR experiments (125 μm vs. 100 μm) in order to accommodate the additional distance traveled by the radiation shock between the end of a VISAR experiment and peak capsule velocity ($CR \sim 4$), which could eject gold into the line–of–sight, if the cone were too thin. Second, we place a 2–3 μm thick coating of parylene plastic on the inner surface of the cone, to tamp the gold blowoff arising from ablation of the inner cone surface due to the M–band radiation that passes through the capsule. Simulations shown in Fig. 9 indicate these modifications are sufficient to prevent these two failure modes.

C. Perturbations

The sinusoidal ripple machined on the capsule is not visible in an initial time radiograph. A successful measurement requires timing the radiographs to be taken after the contrast has grown to a diagnosable level. The relevant metric is the modulation of the optical depth, defined as the first harmonic of the radiograph lineout. The optimal window for diagnosability is an OD modulation approximately between 0.05 and 0.5. For comparison, the initial OD modulations (calculated

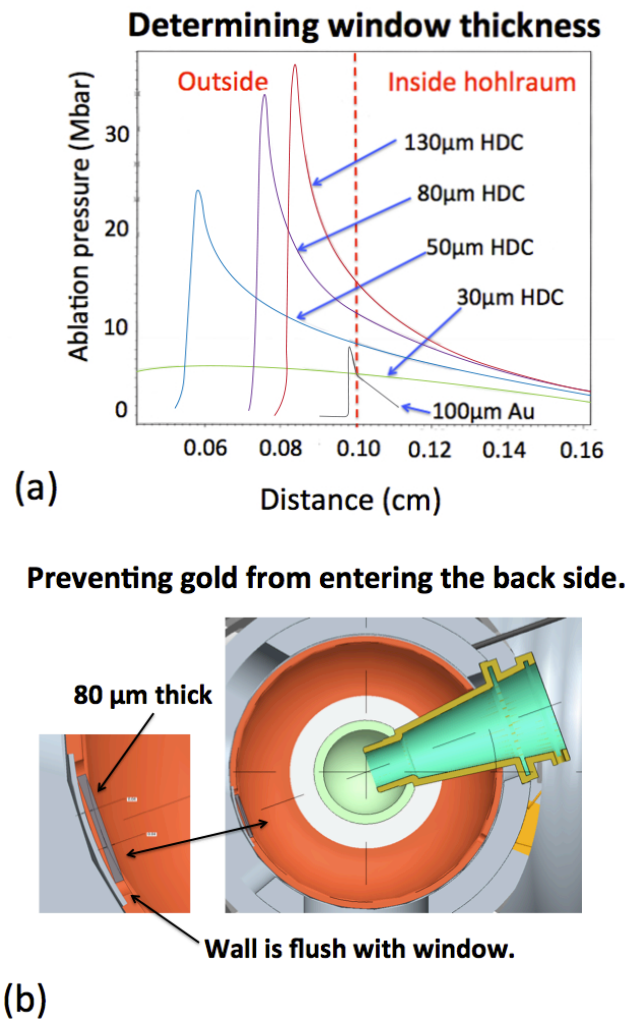

FIG. 7: (a) 1D simulations indicate an 80 μm high–density carbon (HDC) window thickness is sufficient to keep the diagnostic line–of–sight open for the duration of the experiment. The dashed line is the initial position of the inner surface of the hohlraum wall and the windows are mounted to be flush with this inner surface. The simulated curves plot the ablation pressure versus distance for different HDC window thicknesses and a 100 μm thick gold hohlraum wall at the time corresponding to capsule $CR = 2$. At 21 ns, the ablation front in the gold has moved somewhat to the left while the ablation front of the window is actually outside the hohlraum. What keeps the line–of–sight is kept open is the pressure of the HDC blowoff being everywhere higher than that of the gold. By this criterion, an 80 μm thick window is sufficient, while a 30 μm window could possibly fail. (b) The usual 130 μm thick window is thicker than the 100 μm hohlraum thickness on the equatorial "diagnostic band". Simply substituting the thin window leaves a possibility of gold entering the line–of–sight from the back side. Therefore, we thin the diagnostic band by 20 μm in the vicinity of the window to obtain a flush surface.

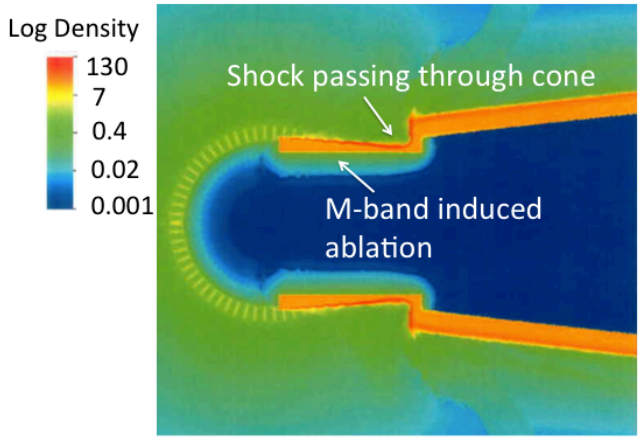

FIG. 8: Two cone–related ways by which gold could enter the line–of–sight. Gold could be ejected into the line–of–sight by the radiation shock burning through (unless the cone were sufficiently thick) or ablated into the line–of–sight due to M–band radiation passing through the capsule. Both of these failure modes are related to our experiment running longer in time than keyhole shock timing experiments and without the liquid deuterium fill, which would tamp away these effects.

as discussed at the end of Section II) for the perturbed capsules in our experiment (see Table I) range from 0.00035 to 0.0025. The lower diagnosability limit is based on being sufficiently higher than the instrument noise, after the instrument response has been accounted for; we measure the noise to be around 0.01 for the low–foot shots and somewhat higher for the high–foot shots. The upper limit is based on having sufficient transmission through the spike to clearly infer the first harmonic, and its precise value depends on the overall transmission [88]. The radiograph timings are chosen to span the optimal window, ensuring at least one image even if the actual growth is much larger or smaller than prediction.

Figure 10 shows the predicted OD modulation versus time (for a 5.4 keV vanadium backlighter) of a mode 60 perturbation ($\sim$ 120 μm initial wavelength) for a number of initial amplitudes. The initial amplitude determines the largest radius for which a mode is diagnosable and also the highest convergence for which the growth is close to linear, believed to be the case relevant for ignition targets [17]. For a given mode number, the strategy for diagnosability is to pick the largest initial amplitude for which the predicted growth is still close to linear at the experiment radius. For example, a 1.5 μm initial amplitude is suitable for measurements between 18 and 20 ns, but nonlinear saturation is apparent at later times. The smallest initial amplitude shown here, $\sim$ 50 nm, only crosses the noise threshold (0.01) at 20 ns and saturates just before 22 ns, near the end of the acceleration. For a typical target, the mode 60 component of the surface roughness has an amplitude $\sim$ 3 nm [18]. By extrapolating the curves in Fig. 10 to this amplitude, we see the predicted growth is close to linear throughout the acceleration but the signal becomes higher than the noise level only past 21 ns [89]. Some design considerations specific to our use of a layered ablator, as opposed to one with uniform composition, are discussed below in Section V.

Table I lists the actual perturbations and capsules used in the experiments. The shot sequence begins at low convergence ($CR \leq 1.5$) with large initial amplitudes and continues at

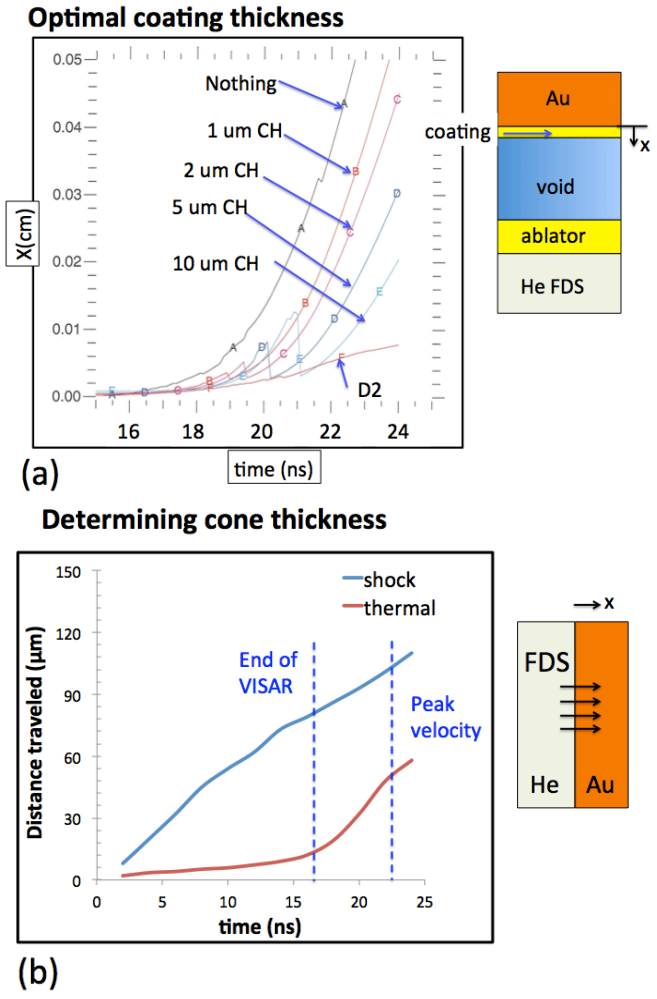

FIG. 9: (a) 1D simulations indicate (a) that a 2–3 μm parylene plastic (CH) coating on the inner cone surface sufficiently tamps the gold blowoff arising from ablation due to M–band radiation passing through the capsule and (b) that increasing the cone thickness from 100 μm to 125 μm accommodates the additional distance traveled by the radiation shock between the end of a keyhole shock timing experiment and peak capsule velocity ($CR \sim 4$). In both cases, a frequency–dependent radiation source (FDS) is applied in the hohlraum gas (helium) region, as depicted. In (a), the distance X is the blowoff density, either due to gold or the plastic coating, at which the optical depth over the length of the cone is as large as a single surface of the capsule (which would nullify much of the advantage of doing single pass radiography). The criterion was for X to be much less than the 400 μm radius of the cone opening for the $\sim$ 22 ns duration of the experiment. In (b), the distance is the position of the shock or thermal wave relative to the initial interface.

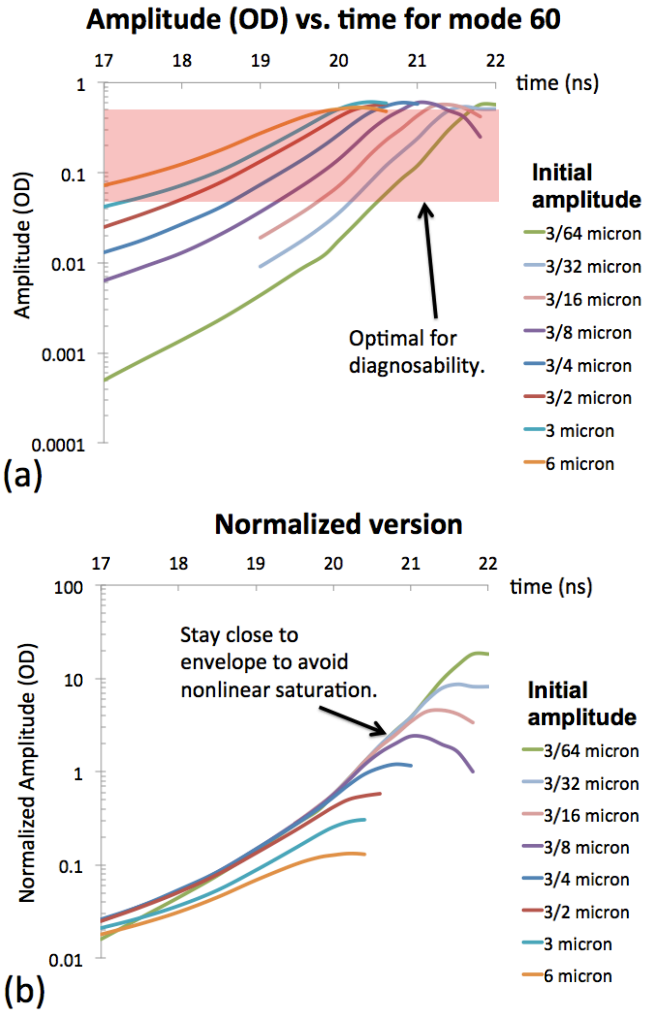

FIG. 10: Pre–shot simulations for the growth of mode 60, for a low–foot drive, for various initial amplitudes. (a) Amplitude (OD) versus time is given with the optimal window for diagnosability shown. (b) The same curves as (a), but normalized to the 1.5 μm curve (e. g. each curve in (a) is multiplied by 1.5 μm divided by the initial amplitude), show the larger amplitudes deviating from the linear envelope at earlier times.

higher convergence ($CR > 2$) with smaller initial amplitudes. The purpose of the low convergence, large radius experiments is to investigate the end of the RM phase, which sets the initial condition for the RT stage, as well as to ensure, during platform qualification, that the perturbations are clearly resolvable within the 20 μm spatial resolution of the diagnostic, as the perturbation wavelength decreases with convergence. The higher convergence experiments involve two different wavelengths side–by–side, which also permits a determination of the phase of the growth, as discussed below and in Appendix A.

Fig. 11a shows an atomic force microscope trace of a capsule surface with modes 60 and 90 side–by–side. Simulations determined that for the modes studied in the present work, a modal purity requirement of 10% on the second and third harmonics is sufficient for the other modes not to influence the growth of the fundamental. The manufacturing process involves first cutting a 2–4 μm deep recession groove, to define a spherical fiducial surface prior to machining the ripple on a lathe. As shown in Fig. 11a, this process often leaves a slight low mode structure superposed on the rippled region (in this case, the recession depth is asymmetric as well) which, simulations indicate, will not influence the measurement as long as

the main ripple grows significantly faster than this low mode structure (usually the case by design). Simulations shown in Fig. 11bc indicate the groove, itself a large perturbation, does not interfere with the central ripples, and that potential edge effects are further mitigated by having a shallow transition width.

IV. EXPERIMENTS

The aim of the first experimental campaign is to measure the instability growth versus Legendre mode number for two ignition–relevant pulse shapes. The first is a low–foot drive for high–gain ignition, representative of what was fielded during NIC. Our specific low–foot pulse was previously used in the N120321 shot which achieved the highest fuel compression of any shot to date [38] and has also been the focus of extensive modeling work [18, 19]. The second pulse is a high–foot drive, which trades one–dimensional ignition margin for additional margin in a number of respects, including much lower instability growth. Our specific high–foot pulse is based on the lowest energy member of the high–foot series [2, 3], and is related to the shots which produced the highest neutron yields to date [39], nearly 10 times higher than what was achieved during NIC.

The instability mitigation property of the high–foot pulse is shown in Fig. 12. Figure 12 compares the density fields at $CR \sim 2$ of initially identical capsules perturbed with modes 60 (top) and 90 (bottom), for the low–foot and high–foot drives. The high–foot drive gives noticeably less growth for both modes, the increased stability being due, in part, to a smaller density gradient [12, 90] at the ablation front, also apparent in the figure. Our simulations indicate the density gradient scale length, $L_\rho \equiv \rho/|\nabla\rho|$, is roughly a factor of three larger for the high–foot drive (e. g. $\sim 30\mu$m vs. $\sim 10\mu$m). Fig. 12b compares simulated (linear) optical depth growth factor curves (calculated as discussed in section II) for the two pulse shapes at $CR \sim 2$. These curves show peak growth occurring around Legendre mode 60 for both pulses and that the high–foot drive gives increased stability for a broad range of mode numbers.

The time evolution of the wavelength, which is proportional to the radius (e. g. $\lambda = 2\pi R/l$, where l is the mode number and R the capsule radius), is a measure of the capsule trajectory and provides an independent check on the model radiation sources. The wavelengths are determined by analyzing a three ripple region (for the side–by–side targets, this is done for each mode) near the center of the image. The reason for focusing on only the central part of image is to minimize the uncertainty due to the radiograph being a planar projection of a spherical capsule surface (as well as effects from the additional low mode curvature due to the manufacturing process, as shown in Fig. 11a), where the spikes are viewed at an angle. This is the dominant uncertainty for the wavelength measurement and is greater for longer wavelengths and larger amplitudes. Figure 13 shows the model trajectories are usually within error bars, and always within "2σ". We can put all of the low–foot (high–foot) wavelength measurements on the

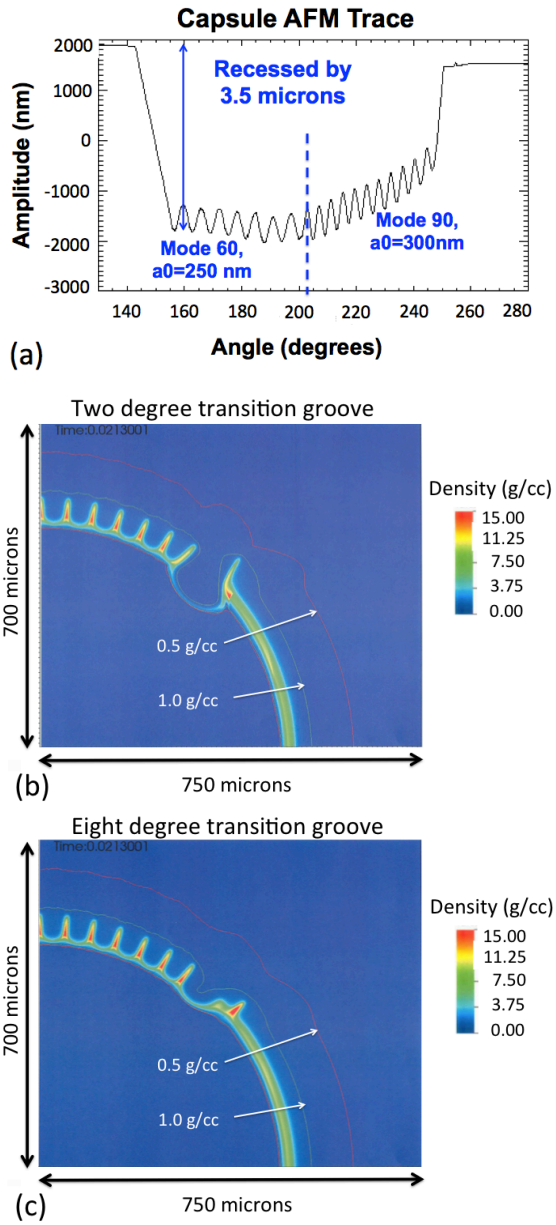

FIG. 11: (a) Atomic force microscope trace of a capsule surface, illustrating that the two modes are connected together at a maximum (the joint indicated by the dashed line), and also the few micron recession groove that is required by the manufacturing process. (b) and (c) show the effect of the recession groove for a (b) steep and (c) shallow transition. The simulations predict the central ripples grow undisturbed by the groove in both cases, while the edge effects may be mitigated by having a shallower transition, with 8–10 degrees being sufficient. If the growth is much larger than simulated, the edge effects could influence the measurement, either by directly disturbing the central ripples or indirectly by providing a pathway for radiation to get inside the capsule. With the current manufacturing process, it is not possible to make the transitions on both sides of the groove arbitrarily shallow, so the targets have an 8–10 degree transition on one side (left side of (a)) and a few degree transition on the other (right side of (a)).

	Nominal	N130602	N130702	N130715	N130718	N130722
Capsule parameters						
Outer radius (μm)	1137	1123.78	1116.67	1122.10	1122.74	1130.84
Thickness (total) (μm)	209	208.35	209.34	206.27	206.37	209.24
Thickness, layer 1 (μm)	20	20.24	20.05	19.26	19.05	19.75
Thickness, layer 2 (μm)	6	6.12	7.5	6.22	5.82	5.83
Thickness, layer 3 (μm)	35	34.36	33.08	35.25	35.64	34.96
Thickness, layer 4 (μm)	10	10.27	10.76	10.76	10.76	10.57
Si atom fraction, layer 1 (%)	0	0	0	0	0	0
Si atom fraction, layer 2 (%)	2	1.98	1.76	1.76	1.76	1.98
Si atom fraction, layer 3 (%)	4	3.72	3.72	3.72	3.72	3.72
Si atom fraction, layer 4 (%)	2	1.70	1.70	1.70	1.70	1.70
Si atom fraction, layer 5 (%)	0	0	0	0	0	0
Perturbations						
Mode 1 (nominal)	–	60	60	60	60	30
Mode 1 (actual)	–	59.1	59.1	57.1	59.1	29.7
Initial amplitude (μm)	–	1.69	1.74	0.24	0.24	0.93
Initial wavelength (μm)	–	119	118	123	119	238
Mode 2 (nominal)	–	–	–	90	90	–
Mode 2 (actual)	–	–	–	85.7	89	–
Initial amplitude (μm)	–	–	–	0.30	0.31	–
Initial wavelength (μm)	–	–	–	82	79	–
Recession depth (μm)	–	3.5	3.5	3.5	2.5	3.5
Laser						
Pulse: Low–foot (LF) or High–foot (HF)	–	LF	HF	LF	HF	LF
Is pulse compensated for missing BL beams?	–	N	Y	N	Y	N
Power deviation in picket (%)	0	-6.5	-2.8	-5.6	0.6	-7.6
Power deviation in trough (%)	0	-6.5	-2.6	-5.9	0.	-8.4
Power deviation in 2nd (%)	0	-4.4	–	-5.6	–	-7
Power deviation in 3rd (%)	0	-1.7	-1.4	-3.1	0.4	-4.7
Power deviation in 4th (%)	0	-2.5	-3.3	-5.6	-3.1	-3.6
Backlighter Energy (keV)	5.4	5.4	5.4	5.4	5.4	5.4

TABLE I: Table of as–shot capsule parameters, laser parameters, and perturbations. Nominal values are given for reference. The different parts of the laser pulse are explained in a number of references, including Ref. 31.

same plot if we scale by the initial wavelengths. That the data essentially fall on the same curve on the scaled plot demonstrates that shot–to–shot variations in the laser and capsule do not significantly influence the trajectory. On the scaled plot, the simulations are consistent with the spread in the data.

Fig. 14 shows images and lineouts, at roughly the same radius around $CR \sim 2$, for the two shots having modes 60 and 90 side–by–side. Given the capsules were nominally identical, the final image comparison is visually striking: both modes show significant growth with the low–foot pulse while for the high–foot pulse, there is visibly less contrast for mode 60 and mode 90 hardly rises above the noise. The lineouts indicate that both modes have grown with positive phase as the two modes, initially connected at a maximum (see Fig. 11a), are still connected at a maximum, corresponding to a spike in the radiograph. If both modes would have inverted phase, the connection joint would also have inverted, becoming a bubble. If one mode would have inverted, there would be a transition region, arising from attempting to connect a spike of one mode with a bubble of the other, that is not seen in the data. An expanded discussion of these aspects and how we determine the phase in the radiographs is given in Appendix A.

Figures 15–18 compare the measured and simulated amplitude (OD) versus time and versus wavelength for all of the shots. In these figures, the instrument response has been removed from the data, by dividing the data by the value of the modulation transfer function (MTF) for a 20 μm slit at the measured wavelength, and compared with ideal simulations. The experiment wavelengths are mostly in the regime where the MTF is well characterized (the uncertainty is no more than 10%) and larger than 0.5, except for the highest convergence mode 90 data, i. e. the 21.0 ns point of Fig. 16b and the 15.2 ns point in Fig. 17b. The measurement uncertainty on the amplitude (OD) is nominally 20%, which is comparable to the size of the data points in these figures.

Figure 15 plots results from the mode 30 experiment. Except for the latest time data point, the model is within the error bars on the time comparison and within "2σ" (of the wavelength uncertainty) on the wavelength comparison. For the 21.0 ns data, the model overpredicts the growth by about 30% on the time comparison and around 50% on the wavelength comparison. We note that for the mode 30 shot, the laser power deviation is anomalously large compared to the other experiments (see N130722 column of Table I) as four beams needed to be dropped due to facility issues during the shot. It is possible that our simplified method of adjusting for the measured power deviations, discussed in section II, may not fully capture the effect of such a large deviation and, in order

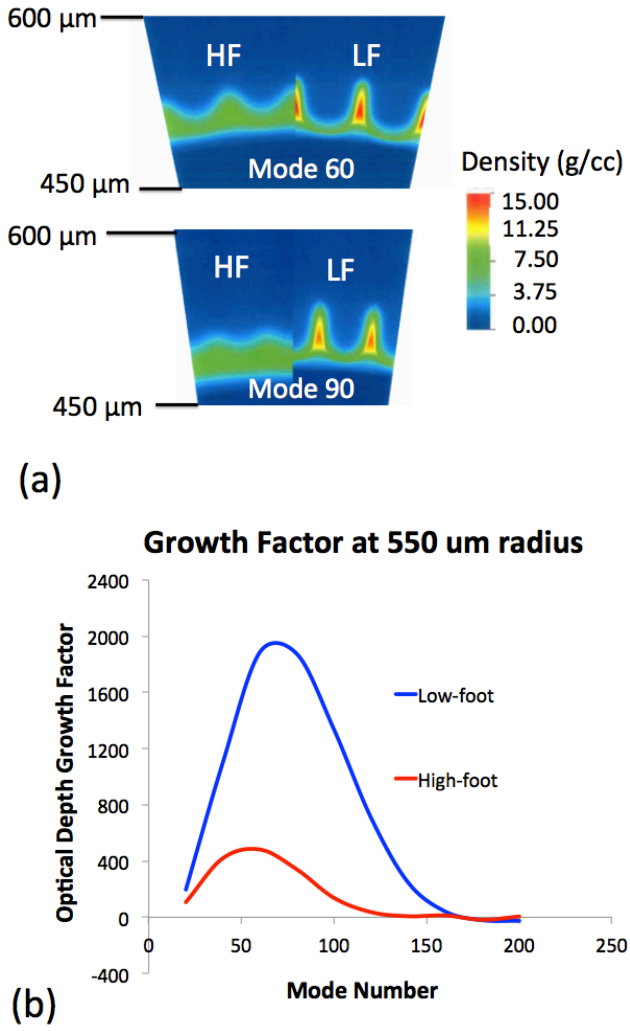

FIG. 12: (a) Simulated densities for modes 60 ($a_0 = 0.24\mu$m) and 90 ($a_0 = 0.3\mu$m) for the high–foot (HF) and low–foot drives (LF) at 550 μm capsule radius ($CR \sim 2$). (b) Optical depth growth factors for the two pulses at the same radius for a 2xSi capsule.

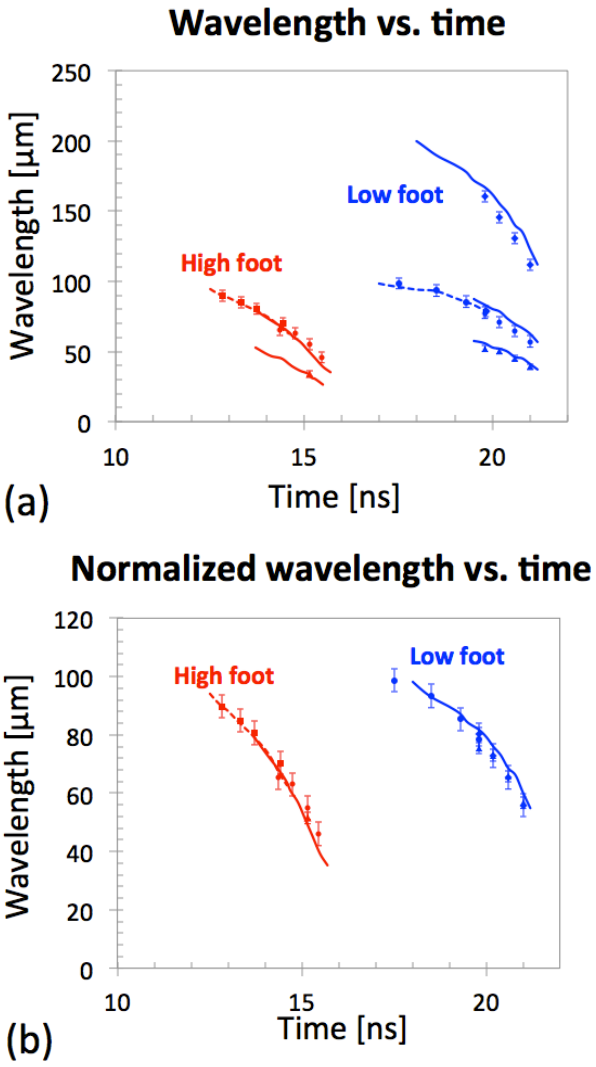

FIG. 13: Comparisons of measured (symbols) versus simulated (lines) evolution of the wavelength. (a) Post–shot model comparisons; (b) Same as (a) except all wavelengths have been scaled to mode 60.

to match the data at later times, a full hohlraum simulation may be necessary to assess the impact of the missing beams.

Figures 16 and 17 plot the measured growth of modes 60 and 90 versus time for the low–foot and high–foot pulses. For mode 60, data from the low convergence, single mode experiments (shots N130602, N130702 in Table I) are shown on the same plot as the mode 60 data from the dual mode experiments (shots N130715, N130718 in Table I), which looked at higher convergence, by normalizing the measurements (and models) by the respective initial perturbation amplitudes. If the growth is linear, the data would fall on the same curve when plotted this way. In both figures 16a and 17a the latest time point of the low convergence data falls below the earliest time point of the higher convergence data, taken at the same time. This indicates nonlinear saturation of the low convergence perturbation, which has a much larger initial amplitude. For both pulses, the model agrees well with the mode 60 data.

The model underpredicts the low–foot mode 90 growth (Fig. 16b) at the earliest time by close to a factor of two, though the other data points are within 25%. On one hand, this could be an actual modeling discrepancy that becomes hidden at later time by nonlinear saturation of the data. On the other hand, when the amplitude (OD) is plotted as a function of wavelength (Fig. 18), which we will discuss momentarily, the agreement is very good so it is also possible that the early time discrepancy is simply a consequence of the uncertainty in the trajectory. A mode 90 experiment optimized for earlier times would be useful in resolving this issue. The model also overpredicts the growth of high–foot, mode 90 (Fig. 17), though it is difficult to draw firm conclusions since only one frame yielded data clearly above the noise.

Figure 18 plots the mode 60 and 90 growth versus wavelength, which permits us to place the low–foot and high–foot data on the same plot. The growth reduction for the high–foot

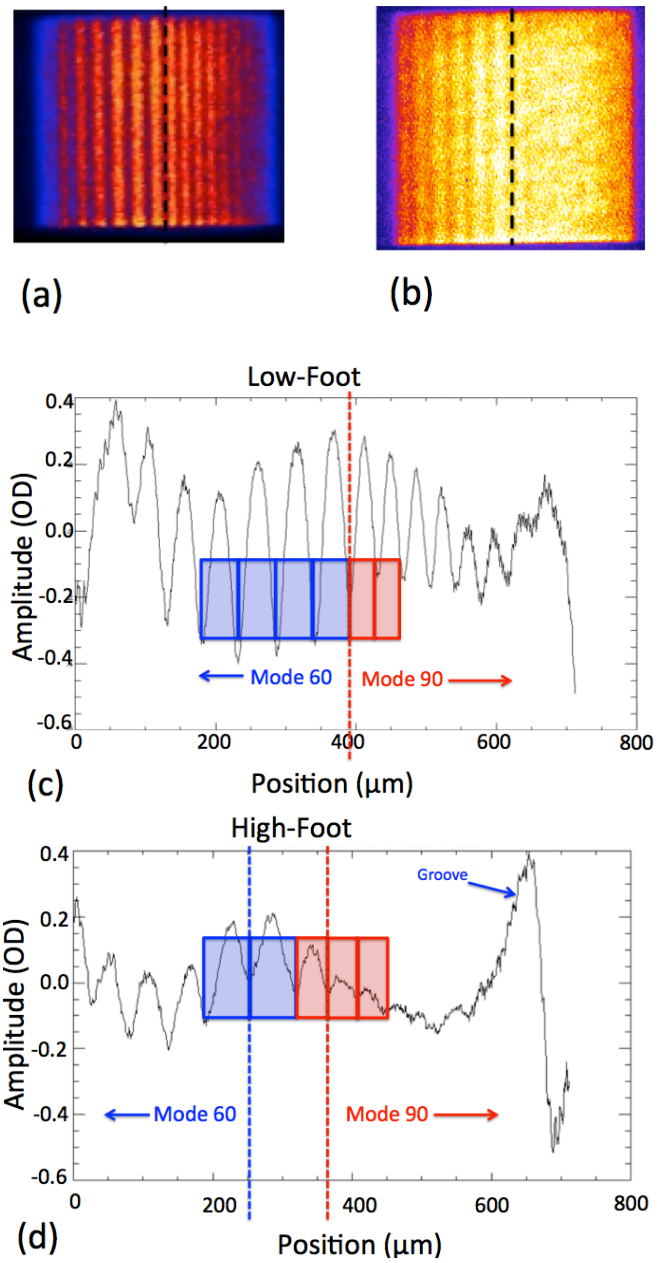

FIG. 14: The slit images show the instability growth arising from nominally identical capsules, with modes 60 and 90 side–by–side, for the (a) low–foot and (b) high–foot drives. The corresponding line outs, (c) and (d), indicate that the modes are still connected at a spike for both drives, implying that for both drives, the modes have grown with positive phase. The comparisons are done at approximately $CR \sim 2$ or 550 μm radius for both drives, corresponding to 21.0 ns for the low–foot drive and 14.8 ns for the high–foot.

drive, measured in terms of optical depth, is 2–4× less for mode 60 and at least 10× less for mode 90. The uncertainty in extracting a definite number for mode 60 is due to the error bar on the measured wavelength and also nonlinear saturation [6, 82, 83], which happens sooner for the faster growing low–foot case, giving the high–foot growth time to "catch up".

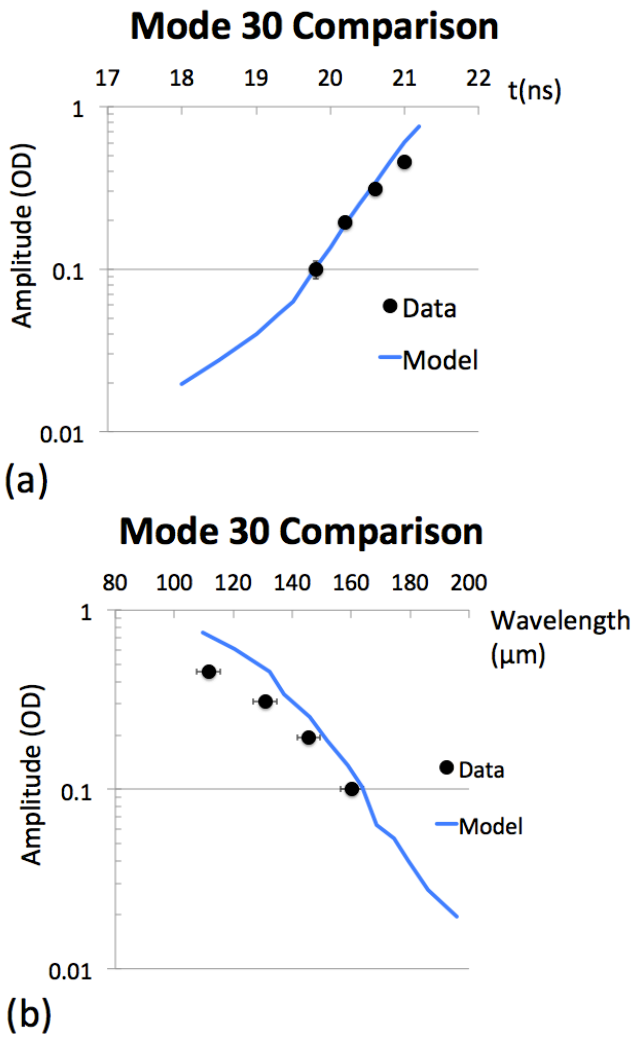

FIG. 15: Amplitude (OD) versus (a) time and (b) wavelength for the low–foot drive. The initial perturbation is mode 30, initial amplitude 0.93μm and initial wavelength 238μm. Complete capsule details are in the N130722 column of Table I.

We will quantify the influence of the nonlinearity in section V.

V. DISCUSSION AND FUTURE WORK

The previous section shows that, for the most part, the model agrees well with the measurements. While the agreement is not perfect, there is no evidence of a 3-5× underprediction of the growth [18] that was of serious concern pre–shot, at least for modes less than 90. We now show that these discrepancies are consistent with the uncertainty in the simulations which, as discussed in section II, is dominated by the uncertainty in the frequency–dependent radiation sources. In particular, the sources are calibrated to match a variety of experimental data which introduces two types of uncertainty into the modeling: the uncertainty in the calibration data and the uncertainty due to the calibration process.

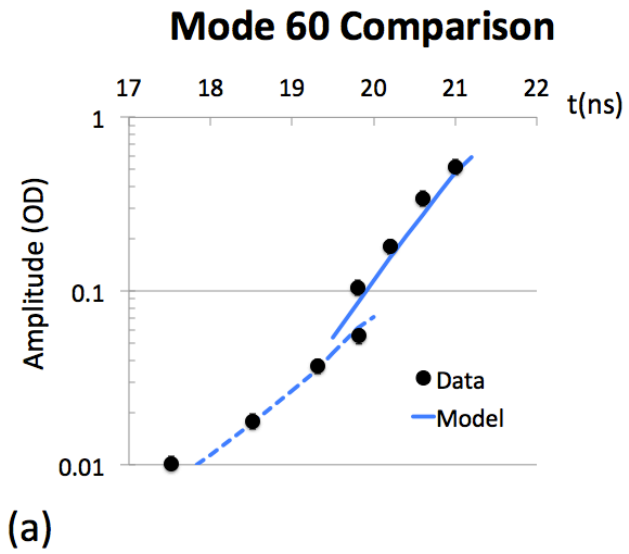

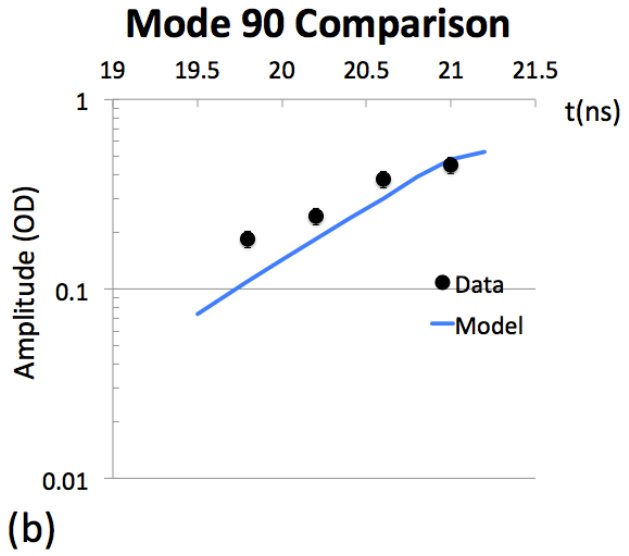

FIG. 16: Amplitude (OD) versus time for modes (a) 60 and (b) 90 for the low–foot drive. The mode 60 data are results of two shots with different initial amplitudes: N130602 ($a_0 = 1.7\mu$m) and N130715 ($a_0 = 0.24\mu$m). The larger amplitude data and post–shot simulation (dashed line) have been scaled by its initial amplitude to appear on the same plot. The mode 90 data is from N130715 ($a_0 = 0.3\mu$m), where this perturbation was machined side–by–side with the mode 60, as shown in Fig. 11a. Further capsule details are listed in Table I.

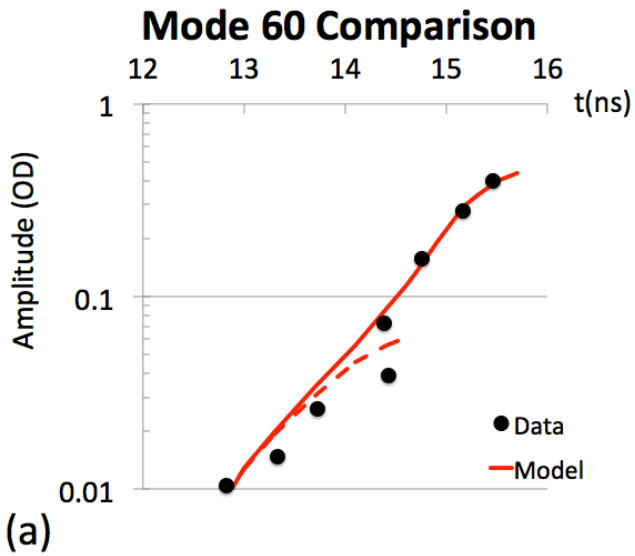

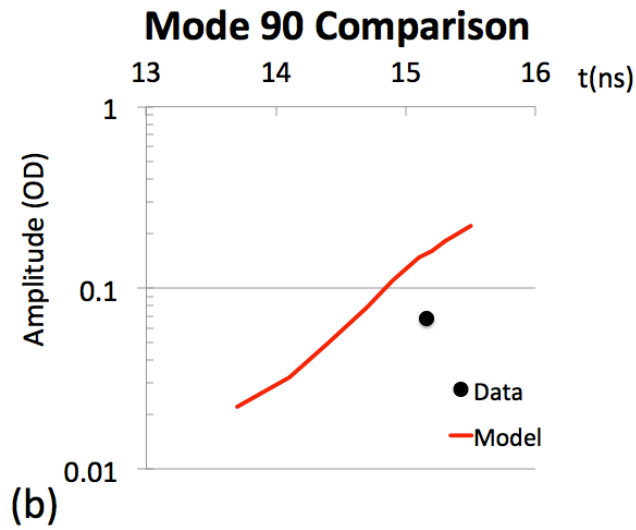

FIG. 17: Amplitude (OD) versus time for modes (a) 60 and (b) 90 for the high–foot drive. The mode 60 data are results of two shots with different initial amplitudes: N130702 ($a_0 = 1.7\mu$m) and N130718 ($a_0 = 0.24\mu$m). The larger amplitude data and post–shot simulation (dashed line) have been scaled by its initial amplitude to appear on the same plot. The mode 90 data is from N130718 ($a_0 = 0.31\mu$m), where this perturbation was machined side–by–side with the mode 60, as shown in Fig. 11a. Further capsule details are listed in Table I.

Of the data entering the calibration, one of the most uncertain is the brightness of the M–band (i. e. $h\nu > 1.8$keV) part of the drive spectrum, which is only known to 30%–50% accuracy [91]. A larger M–band component increases the density gradient scale length, which stabilizes the RT growth [12, 90]. Figure 19 replots Fig. 18 with additional simulation curves where the source M–band fraction has been varied by $\pm 33\%$. All of the experimental data, within error bars, fall inside the uncertainty band defined by these curves. The curves suggest the growth factor modeling uncertainty due to the M–band fraction is no more than 50%. It is possible that the overall uncertainty in the instability growth due to calibration inputs is not much higher than 50%, as previous studies [17] have identified the M–band uncertainty as a dominant contributor. However, further studies are needed to assess this more carefully.

Regarding the calibration process, Fig. 20 plots our results in terms of linear growth factor versus mode number at different capsule radii. In these plots, the data have been multiplied by a factor discussed in Appendix B (in addition to removing the instrument response, as discussed in the previous section),

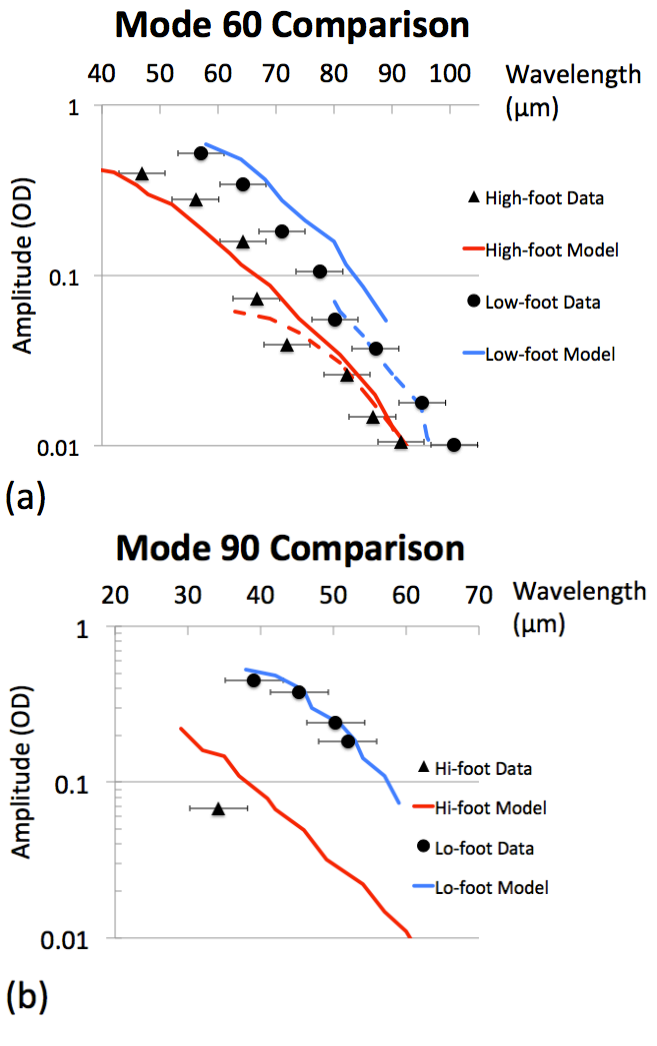

FIG. 18: Amplitude (OD) versus wavelength for modes (a) 60 and (b) 90, comparing results for the low–foot and high–foot drives.

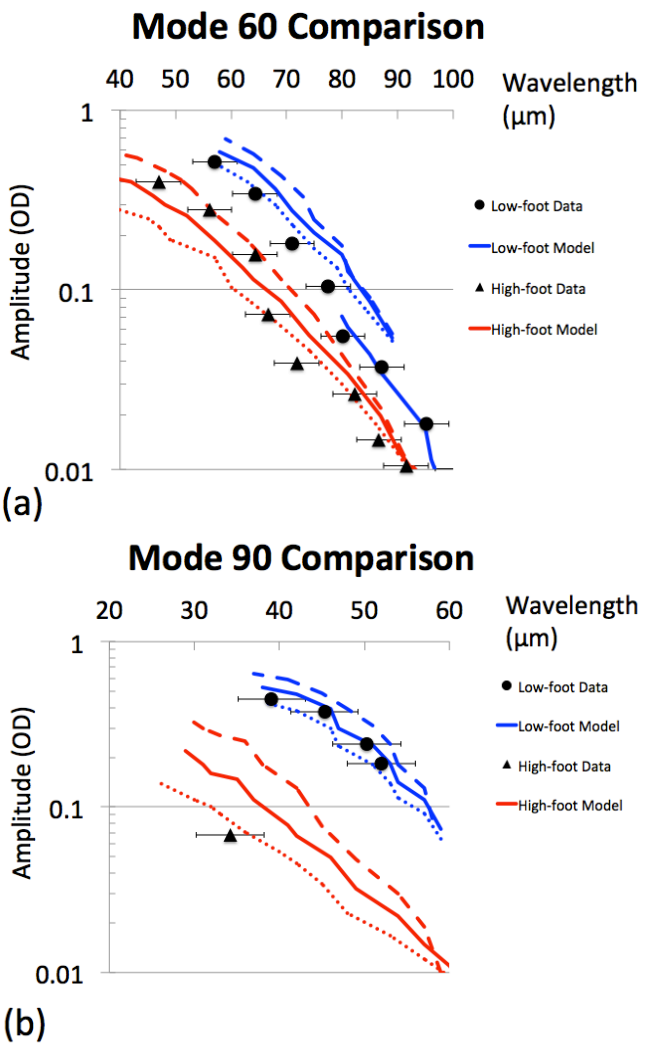

FIG. 19: Amplitude (OD) versus wavelength for modes 60 and 90. The solid lines are the baseline simulations drawn previously. The dashed (dotted) have M–band fractions which are 33% lower (higher) relative to the nominal source.

in order to account for the growth slowing down due to nonlinear saturation and to adjust for differences between as–shot and nominal parameters; the error bars on the data include the uncertainty in this correction factor. Due to the agreement in Fig. 13, the data and simulation are compared at the *time* that the simulation indicates the capsule is at the given radius.

The simulated curves correspond to different radiation source representations of the drive. The curves labeled "baseline" are the models used for comparisons in the previous section. The baseline radiation sources, and the sources used to generate the curves labeled "Low (High) Foot Drive 1" and "Low (High) Foot Drive 2", are fully consistent with the drive calibration framework discussed in section II and in Ref. 18. For comparison, we have also plotted a low–foot drive labeled "Coarse Tune", which is also calibrated to match the implosion features, though less stringently, in a sense we will now describe.

The most constraining step of the drive calibration framework is tuning the source to match the shock velocity trace, within error bars, from the most accurate channel of the relevant VISAR experiment, as shown in Fig. 21 for the low–foot drive. In this figure, the fine–tuned curve is our low–foot baseline source. The coarse–tuned drive is tuned to a match the trace from a less accurate VISAR channel (not shown), where the error bars are more than twice as large, but, as the figure shows, is often outside the error bars of the most accurate channel. Figure 20 shows the three fine–tuned sources being closer to the data, and also to each other, than the coarse–tuned source. This suggests that having a drive that reproduces the shock dynamics very accurately as prescribed in Ref. 18, as opposed to approximately, is essential for modeling this experiment.

The curves based on the different fine–tuned low–foot drives differ from one another at the $\sim$ 20–40% level. "Drive 1" is tuned for a different ablator equation–of–state table, LEOS 5370, than the baseline model, which uses LEOS 5400, but is otherwise constructed in the same way. Both tables

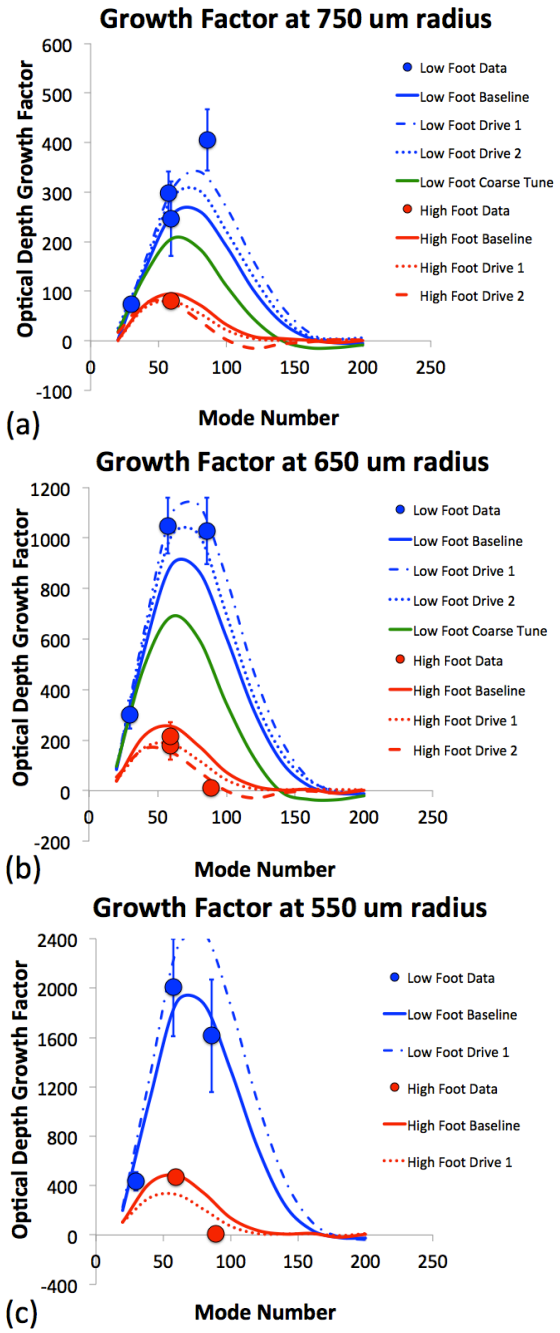

FIG. 20: Optical depth growth factor versus mode number at (a) 750 μm radius (t =19.8 ns, low–foot; t = 13.7 ns, high–foot), (b) 650 μm radius (t =20.6 ns, low–foot; t = 14.4 ns, high–foot), (c) 550 μm radius (t =21.0 ns, low–foot; t = 14.8 ns, high–foot).

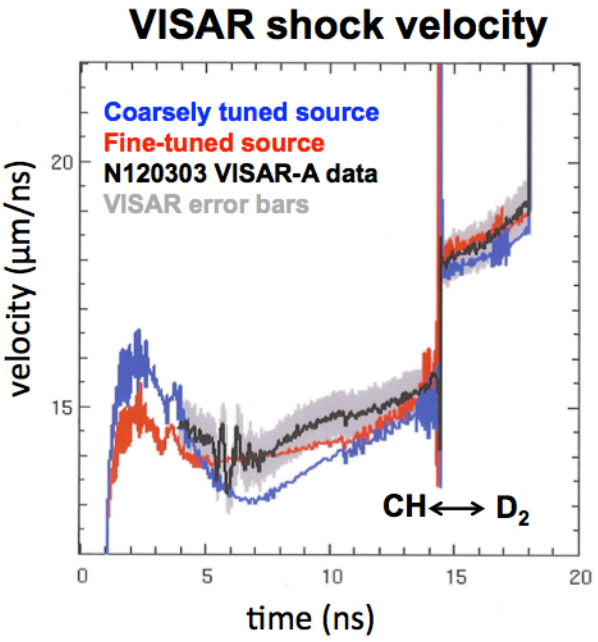

FIG. 21: The most constraining step of the drive calibration process is tuning the source to match the shock timing data within the error bars. The fine–tuned drive is our low–foot baseline model while the coarse-tuned drive is tuned to match a less accurate VISAR channel.

are empirical EOS models for GDP constructed as per the paradigm of Ref. 92 with dissociation models similar to that described in Ref. 93, and fit to experimental data. LEOS 5370 has a softer Hugoniot, based on a different assumption for the appropriate quartz EOS used in analyzing the GDP Hugoniot data of Ref. 94, but the two models are equally valid interpretations given this uncertainty [95]. The tables differ from one another primarily in the density–temperature regime which corresponds to the RM phase of the implosion and the greater instability growth with LEOS 5370 is consistent with its being a less stiff equation–of–state. "Drive 2" also uses LEOS 5370 but, in addition, is calibrated to the most accurate channel of a different VISAR shot, involving a slightly different laser pulse. The different high–foot curves are similar around peak growth factor, but give different predictions for the zero crossing and whether some of the higher modes invert phase. High–foot "Drive 1" uses a different prescription for the M–band part of the drive spectrum. The M–band content of the baseline model is normalized to match recent viewfactor measurements of the high–foot drive, which will be discussed in a separate publication. "Drive 1" uses a different prescription in which the simulations are degraded primarily through multipliers on the thermal part of the spectrum, leaving the M–band part alone, based on results from the low–foot viewfactor [80]. "Drive 2", in addition to using this different M–band prescription, uses a different approach to matching the shock timing data.

The different curves suggest the growth factor modeling uncertainty due to the uncertainties in the equation–of–state model, and the prescriptions for matching shock timing and M–band is no more than 50%. Combined with our estimated uncertainty regarding the calibration data itself, our overall modeling uncertainty is no more than a factor of two, as conjectured in Ref. 17, and possibly much better, at least for the comparatively low mode numbers and small convergence ratios considered so far. There is no evidence of any fundamental problem in computing the instability growth which could result in a 5$\times$ discrepancy or a problem in computing the

phase of the growth, for modes less than 90. An important point is that the models are tuned to match measured implosion features, but not any of the quantities measured in our experiment. Therefore, our results may be viewed as a validation of the overall modeling approach of Ref. 18. Fig. 20 indicates the value of higher mode studies, as all of the models indicate the growth factor sharply decreases at higher modes but give different predictions for the magnitude and phase.

While our experiment was mainly motivated by the possibility of large modeling errors, one may ask if this experiment may be used to probe finer aspects of the modeling, such as distinguishing between the various fine–tuned curves in Fig. 20. While the quality of the data suggests optimism in this regard, a number of issues need to be resolved before embarking on such a program. First, because the tuned source procedure is intended to account for the effects of missing physics, the consequences of using, for example, a less accurate EOS model, might not be apparent if the metric is simply how well a simulation matches our data.

Second, our models involve a number of approximations which need to be improved if we are concerned with resolving differences much finer than a factor of 2. For example, the simulations currently model the radiation transport with multigroup diffusion, but a more accurate transport model, such as implicit Monte Carlo, may be necessary if we are interested in resolving $\sim$ 20% level differences. Similarly, we model the impact of the as–shot laser pulse and missing backlighter beams in a simplified manner (see section II) and ignore the presence of the diagnostic window. Modeling studies [96] have shown that the missing beams and windows could reduce the radiation flux seen by the capsule by as much as 7%, which could influence our results at the 20% level. Also, we have not fully explored the consequences of numerical effects, such as resolution, convergence in radiation binning, impacts of mesh motion and advection, etc.

Finally, nonlinear saturation of the data could make an actual modeling discrepancy appear smaller than it actually is. The procedure in Appendix B, our best estimate of the magnitude of this effect, which involves using the simulation, indicates the perturbations are in the weakly nonlinear regime. Moreover, previous studies of nonlinear saturation in ICF targets [17] have noted that ICF growth factors are fairly independent of the initial amplitude, even when the final amplitudes are comparable to the wavelength. The explanation given in Ref. 17 is that much of the growth is due to Bell–Plesset effects [33, 34], i.e. the perturbations are stretched radially as the wavelength is reduced by convergence, which involves less of the shear–induced rollup phenomena that slows down the growth than in a planar situation with the same amplitude to wavelength ratio. However, a purely experimental assessment of nonlinear saturation is desirable, and perhaps can be achieved in future experiments using targets with two amplitudes of the same wavelength.

Alternately, now that the platform is qualified, the nonlinear effects can be minimized in future experiments by using smaller initial amplitudes. This would also enable studies at higher convergence, which would more stringently test the models and probe conditions closer to when an ICF capsule would ignite. In such a limit, it may be necessary to explicitly model capsule surface non–uniformities [17, 18], which are below the noise at $CR = 2$ (see section III C), but could grow comparable to the seeded perturbation by $CR = 4$, if the growth of the latter slows down due to nonlinear saturation. Also, it may be necessary to carefully account for the asymmetry in the radiation field, which appears to consist mainly of low mode components that become detectable somewhat past $CR = 2$, but produce a clear effect on the capsule shape by $CR = 4$ [20].

We now discuss some potentially confusing aspects of interpreting data from this type of experiment. The experiment measures the amplitude of the OD modulation, which is usually correlated with the amplitude of the modulation in ablator areal density (i. e. $\int \rho dr$). The areal density modulation is the important quantity for instability growth, as the mass redistribution from bubbles to spikes is what leads to the in–flight degradation or break up of the ablator shell. For an ablator with uniform composition, the amplitude (OD) and the areal density modulation are just proportional quantities related by the ablator opacity, while for a layered ablator, the interpretation is less simple.

For a 2xSi capsule, the opacity of the highly doped layer (i. e. the 4% Si layer; see Fig. 22) is roughly 3$\times$ the opacity of the undoped layer. A modulation that is entirely in the undoped layer, a modulation with 1/3 this amplitude that is entirely in the highly doped layer, and intermediate cases, would correspond to different areal density modulations that give the same amplitude (OD) measurement. Figure 22 shows the contributions of the highly doped layer (i. e. the 4% Si layer for a 2xSi capsule; see Fig. 5) and the outer undoped layer to the total amplitude (OD) for a mode 60, $a_0 = 1.5\mu$m perturbation on a 2xSi capsule driven with the low–foot pulse. The model predicts that the problem of an ambiguous data interpretation is confined to the interval between 18.5 ns and 19.5 ns, corresponding to the beginning of the acceleration stage, when both the undoped and doped layers contribute to the OD modulation. Outside of this interval, the modulation is almost entirely in either the undoped or doped layers, making the amplitude (OD) measurement effectively an areal density measurement, with the proportionality constant being either the undoped or doped opacity.

A different potential problem with a layered ablator is illustrated in Fig. 23. In this example, three synthetic radiographs are given for the large perturbation, for the cases of (a) uniform ablator, (b) a 2xSi doping profile, and (c) an extreme profile where the inner layer has $\sim$40$\times$ the opacity of the outer layer [97]. For the uniform ablator, the position of maximum optical depth, or spike in the radiograph, corresponds to the position of maximal areal density. However, in (b), these are offset from one another and in (c), the density maximum at the origin actually lines up with a "bubble" in the radiograph because the x–rays traverse a comparatively smaller path length of the high opacity region.

A different metric of instability growth is the conventional growth factor, as discussed, for example, in Ref. 98, defined as the ratio of the final to initial amplitude of an interface defining the perturbation, such as the ablation front. Fig. 24 shows

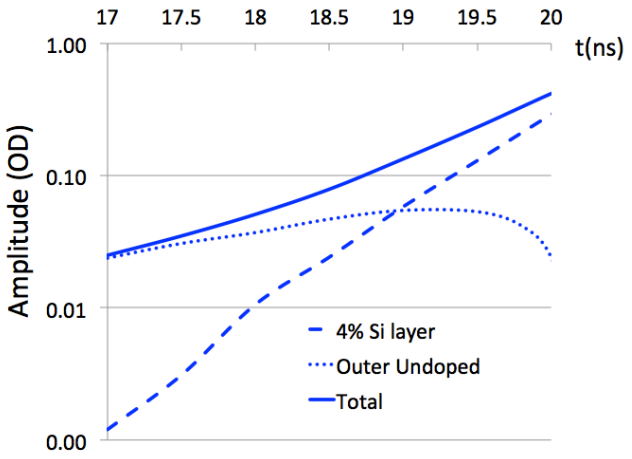

FIG. 22: Growth of a mode 60, $a_0 = 1.5\mu$m perturbation on a 2xSi capsule with the low–foot drive. The curves show the total amplitude (OD), as well as the contributions of the highly doped 4% Si layer and the outer undoped layer as a function of time.

density profiles obtained by applying low–foot drives, differing in the steepness of the rise to peak radiation temperature, to the same perturbed capsule. While (1) has the largest perturbation amplitude, and therefore would appear "least stable" according to the ablation front growth factor metric, (3) has the highest areal density modulation and an amplitude (OD) nearly twice as large as (1). While having a lower areal density modulation is what is important for instability growth, (1) is also less compressed overall, i. e. has lower average areal density, so more analysis is needed to determine whether, as in the high–foot pulse [2], the increased stability results in higher overall performance. The purpose of this example is to illustrate the confusion that might arise from interpreting this experiment, which measures an areal density growth factor, in terms of a conventional interfacial amplitude growth factor.

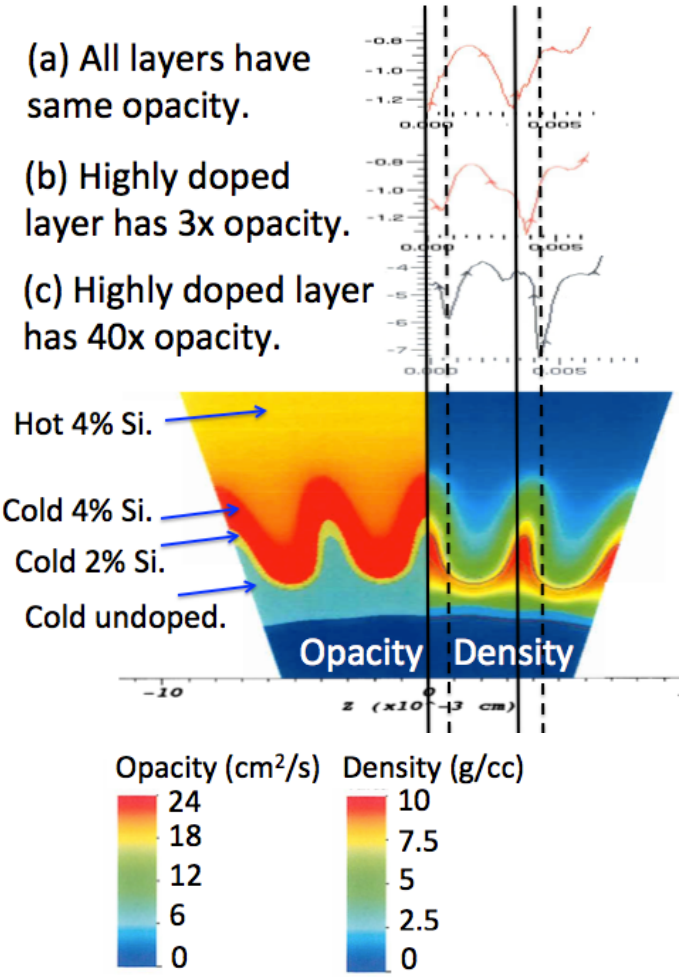

FIG. 23: Three synthetic radiographs of the large perturbation, assuming (a) uniform opacity, (b) a 2xSi doping profile, where the inner layer has $\sim 3\times$ the opacity of the outer layers, and (c) an extreme doping profile where the inner layer has $40\times$ the opacity of the outer layers. Observe how while in (a), the position of maximum areal density lines up with a spike in the radiograph, in (c), it actually lines up with a "bubble".

VI. SUMMARY

A new in–flight radiography capability has been established at the National Ignition Facility (NIF). We have measured the instability growth of 2D sinusoidal ripples, up to a convergence ratio of 4. The growth factors of modes 30, 60, and 90 for a point–design type pulse are close to model predictions, up to convergence ratios around 2. Much lower growth has been observed for modes 60 and 90 with the high–foot pulse, verifying the predicted instability mitigation aspect of the new pulse shape. The results (so far) have largely validated the tuned drive approach to modeling instability growth used at NIF. Experiments in the near term will subject the models to increasingly stringent tests at both higher convergence and higher mode numbers (120 and 160). Future experiments are being designed in this newly qualified platform to investigate a variety of issues that will directly impact ICF capsule performance, including 3D surface roughness, features such as the support tent, instability aspects of alternate ablators and pulse shapes, and more.

Acknowledgments

This experiment was initiated as part of a larger high energy density (HED) ignition science effort led by one of us (O. A. Hurricane) and developed within the mix campaign of the NIF ignition program. We would like to acknowledge M. J. Edwards, A. Hamza, W. Hsing, J. Kilkenny, D. Pilkington, J. Sefcik, C. Verdon, and A. Wan for strongly supporting this project. We would like to thank NIF target fabrication for building the targets and NIF operations for executing the shots. We acknowledge D. Callahan, O. S. Jones, J. Milovich, N. Meezan, and S. Prisbey for discussions about

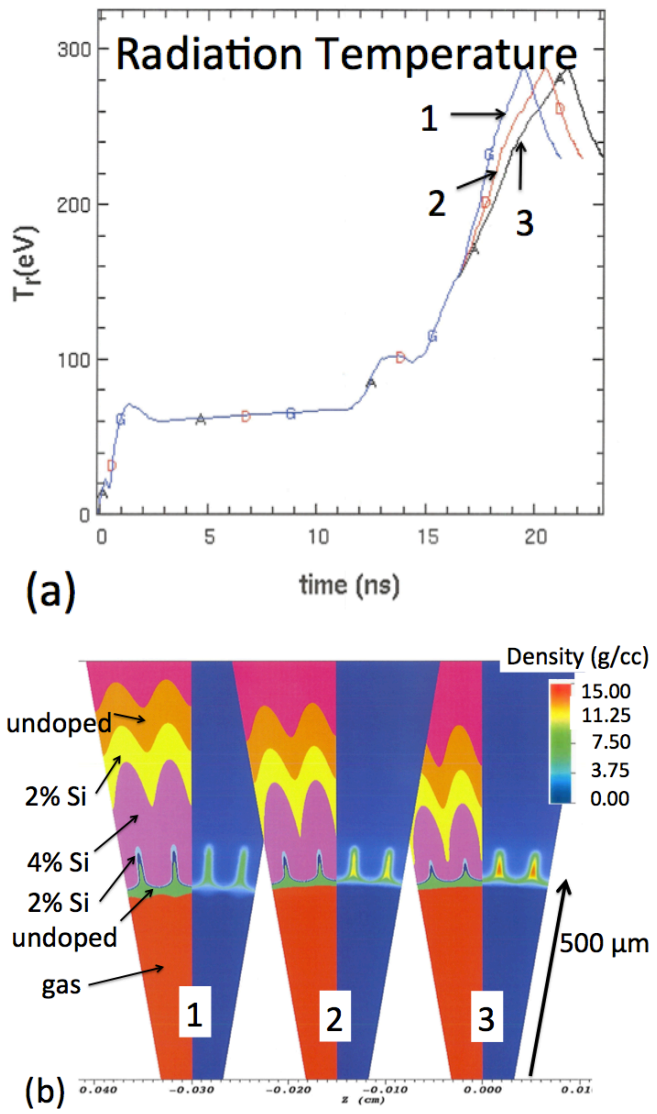

FIG. 24: The three radiation drives in (a) produced the effects shown in (b) on a mode 90, a_0=0.3 μm perturbation. See discussion in main text.

aspects of hohlraum design; N. Meezan for help in determining our pulse shape; S. MacLaren, M. Schneider, and K. Widmann for illuminating discussions about M–band measurements and modeling; and P. Sterne for helpful comments about the GDP equation–of–state. The laser deviations shown in Table I were provided by B. MacGowan. This work was performed under the auspices of the U.S. Department of Energy by Lawrence Livermore National Laboratory under Contract DE-AC52-07NA27344.

Appendix A: Measuring the phase of the growth

A mode is said to have grown positively if maxima (minima) in the initial condition correlate with maxima (minima) in the final pattern. Negative growth, or phase inversion, means maxima in the initial condition line up with minima in the final pattern. Whether or not a mode inverts phase is sensitive to details of the ablator and drive [17, 98–100]. The issue is important for ignition designs because the phase determines whether an isolated bump on the capsule surface will grow outwards as a bump or inwards as a divot (believed to be a worse scenario as this could directly quench the hotspot) depending on whether the modal content of the bump is dominated by positively growing or inverting modes [98].

We determine the phase in our experiment by analyzing the pattern of distances in the radiograph for targets having two different wavelengths side–by–side, which are modes 60 and 90 in the present case. As shown in Fig. 11a, the capsule is machined so that the two modes are initially connected at a maximum, corresponding to a spike in an initial radiograph. Figure 25 shows synthetic radiographs, taken at approximately $CR = 2$, from an idealized simulation, including the recession groove required by the manufacturing process, of the two–mode target driven with the low–foot pulse.

The three scenarios shown are (a) both modes growing positively (which is what the simulations predict), (b) both modes inverting, and (c) just mode 90 inverting (the image shown here is earlier in time than the other two, hence the different spacings). Scenarios (b) and (c) are created by inverting the initial amplitude of one or both modes at the beginning of the simulation. While the latter procedure is motivated by the known sensitivity of the inversion to the early time drive [17, 98–100], we emphasize this is not meant to be a physical mechanism for how inversion actually occurs. The purpose is to demonstrate how the analysis procedure distinguishes between different inversion scenarios, regardless of how the inversion actually happens. [101].

To analyze these radiographs, the first step is to identify the rightmost (leftmost) *spike* that clearly belongs to the mode 60 (90) pattern, based on the distance between it and the adjacent spike to its left (right), which we mark by the dashed lines in these figures. The second step is to analyze the distances between spikes in the region in between these markers. In Fig. 25a, the marker lines fall on the same spike, indicating the modes are connected at a spike as they were initially, which means that both modes have grown positively. In Fig. 25b, the distance between the markers is the average of the mode 60 and 90 wavelengths, indicating both modes have shifted by a half wavelength. This means both modes have inverted and are now connected at a bubble, the connection joint having also inverted. In Fig. 25c, the pattern between the markers is consistent with a half wavelength of mode 90 and a full wavelength of mode 60, indicating just mode 90 has inverted [102]. As the "joint" is now attempting to connect a spike of mode 60 with a bubble of mode 90, we obtain the transition region shown in the figure.

The connection joint in Fig. 25a is readily identified because the two modes are roughly the same size, which is accomplished by giving the slower growing mode (mode 90) a larger initial amplitude (0.3 μm instead of 0.24 μm). In this case, the edge effect due to the proximity of the other mode is essentially confined to the connection joint. If the same capsule is driven with the high–foot drive, we obtain the synthetic

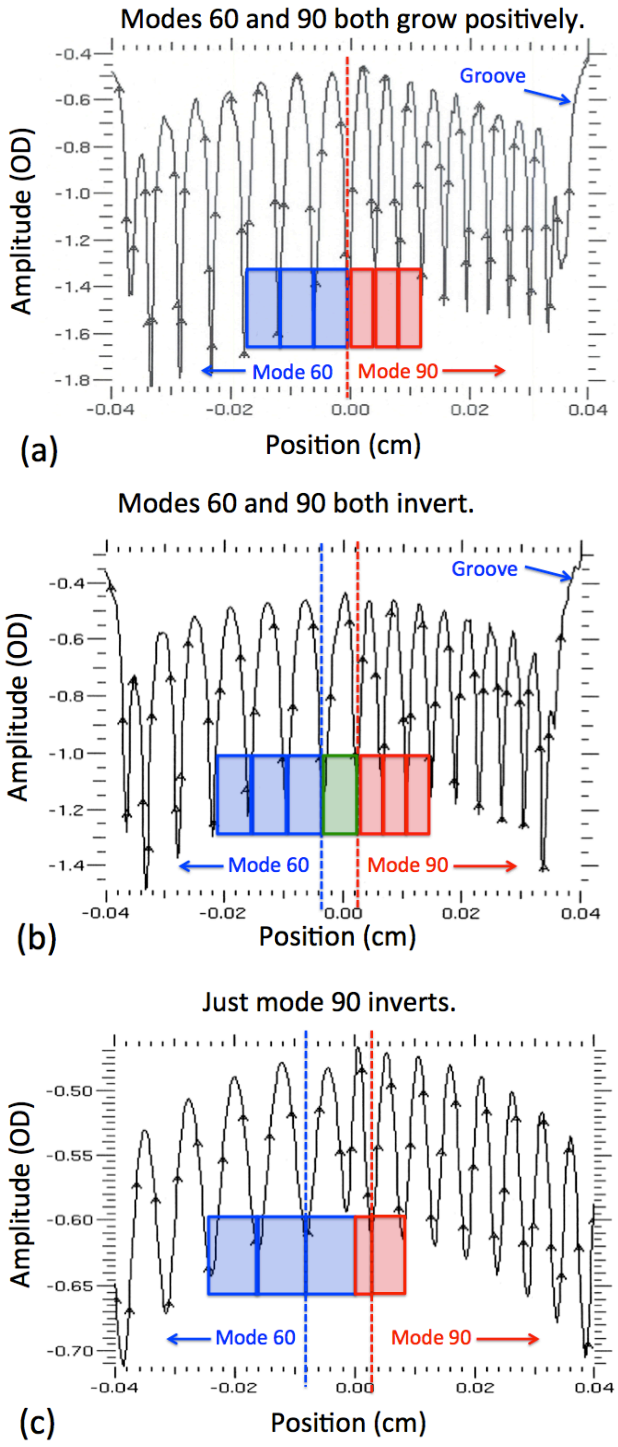

FIG. 25: Synthetic radiographs for the low–foot mode 60–90 shot, showing three scenarios for the phase of the growth, as discussed in the text.

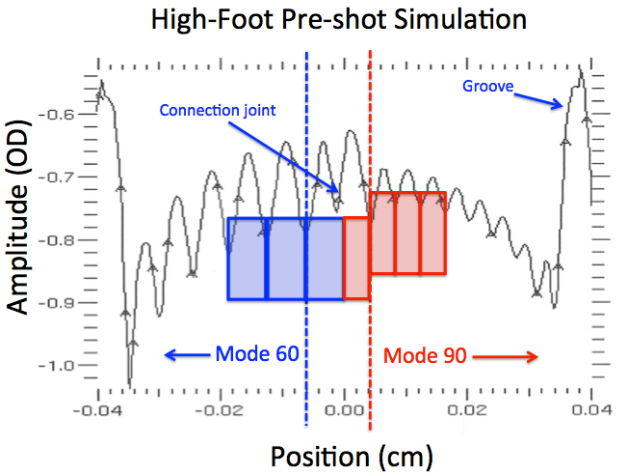

FIG. 26: Synthetic radiograph for the high–foot mode 60–90 shot, which uses the identical capsule as the low–foot experiment. Compare this radiograph with Fig. 25a.

radiograph shown in Fig. 26, which predicts the mode 90 side grows much less. Fig. 26 shows the same analysis as above may be used to infer positive growth for both modes. Because the distance between the markers is exactly the sum of the two wavelengths, the spike in between may be naturally identified as the connection joint, which has slightly moved. There is a large bubble to the immediate right of the joint, which by definition makes it part of the mode 90 pattern, that resembles the bubbles on the mode 60 side (in size); this could be misidentified as a mode 60 feature, if the analysis is not applied carefully.

As shown in Figs. 11bc and Figs. 25–26, the recession groove creates a large bubble, which is a prominent feature in the radiograph that could, in principle, be used as a spatial fiducial for assessing inversion. However, the uncertainty in how to precisely reference this feature to the ripple pattern, along with the uncertainty in the wavelength measurement away from the central region (at least for modes less than 90) discussed in the main text, leads us to prefer the method discussed above. We note that fabrication and alignment difficulties eliminated an external fiducial, such as a thin wire placed on the diagnostic window, as a possible option. Also, our simulations (as well as other studies, such as Ref. 100) predict phase inversion, if it occurs, typically happens early in the RM phase, before the perturbations have reached a diagnosable level. This prevents us from verifying an inversion by simply correlating images taken at different times.

For the large perturbations and fast–growing modes discussed in this paper, the determination of the phase will not be affected by non–ideal capsule features, such as surface roughness or the low mode structure within the recession groove (see Fig. 11a). The surface roughness remains below the noise during the measurement time (see the discussion in section III C) so will not affect our measurement, including the determination of the phase. Similarly, the low mode structure within the recession groove due to the machining process (see Fig. 11a) is predicted to grow much more slowly than the mode numbers studied here. However, accounting for such aspects could be important for higher convergence experiments involving much smaller seeded perturbations. In particular, the interference between a small seeded “cosine” perturbation and a “sine” perturbation at the same wavelength,

that is present in the non–ideal initial condition or generated through nonlinear processes, could lead to arbitrary phase shifts, which would complicate the analysis.

Appendix B: Nonlinearity corrections

The instability growth in an ICF capsule is expected, based on our present understanding of the initial condition and growth rates, to remain in the linear regime throughout the implosion. This is reason why linear growth factor curves, calculated from infinitesimal amplitude simulations as discussed in section II, are commonly used metrics of the instability properties of ignition designs. Therefore, in order to compare our measurements with linear growth factor predictions, we need to correct for nonlinear saturation in the data and to account for shot–to–shot variations in the capsule and drive parameters.

In order to do this, we multiply the data by the following correction factor C before placing the experimental points on the plots in Fig. 20:

$$C = \frac{GF_{\text{linear}}}{GF_{\text{as-shot}}} \tag{B1}$$

where GF_{linear} is the linear optical depth growth factor and $GF_{\text{as-shot}}$ is the (not necessarily linear) growth factor calculated from a post–shot simulation of the actual perturbation, both calculations using the baseline drive. If the growth is actually linear, and if differences between the nominal and actual capsule/drive are unimportant, then C would be unity. Nonlinear saturation would slow down the growth [6, 82, 83] resulting in C being greater than unity. The main justification for using the simulation to estimate nonlinear saturation in the *data* is the general agreement between the models and data presented in Section IV. We nominally use $\pm 0.5 * (C - 1)$ as an estimate of the uncertainty in this "unfold" procedure; the quadrature sum of this and the measurement error determine the error bars on the data shown in Fig. 20. For all of our shots, this factor C is a few percent correction for the first data point, growing to 20–50% by the fourth data point.

As an example, consider the 650 μm radius mode 60 and mode 90 data for the low–foot drive. We can describe the nonlinearity by using a 1D simulation to relate the amplitude (OD) growth to the growth of the amplitude of the ablation front. At 650 μm radius (t=20.6 ns), the measured optical depth growth factors for modes 60 and 90, low–foot, are both around 1000. Of this, a factor of $\sim$3 is simply due to the opacity change from the ablation front being initially in the undoped layer to being entirely in the doped layers. According to Fig. 6a, the density increase is about a factor of 7. Therefore, an amplitude (OD) growth factor of 1000 corresponds to an ablation front amplitude growth factor of $1000/\Delta(\kappa\rho) \approx 50$. For mode 60, the initial amplitude is $a_0 = 0.24\mu$m while the wavelength at 650 μm radius is about 70 μm, so that $a/\lambda \sim 0.17$. For mode 90, the initial amplitude is $a_0 = 0.3\mu$m while the wavelength is around 47 μm, for an experiment time $a/\lambda \sim 0.3$. These estimates suggest mode 60 perturbation is only starting to enter the weakly nonlinear regime [6, 82, 83] while mode 90 is clearly in the weakly nonlinear stage.

To calculate the correction factors, we take the values of GF_{linear} from the low–foot baseline curve of Fig. 20b, which are $\sim$900 for mode 60 and $\sim$800 for mode 90. For $GF_{\text{as-shot}}$, we divide the $t = 20.6$ns values of the simulated amplitude (OD) from Fig. 16 (about 0.3 for both modes) by the respective initial amplitude (OD) values, calculated as discussed in section III C. Therefore $GF_{\text{as-shot}}$ is about 850 for mode 60 and about 700 for mode 90. Hence, the respective correction factors are $C = 1.06$ for mode 60 and $C = 1.15$ for mode 90. That these values are not too far from unity, and the fact that C is less for mode 60, are consistent with the modes being in the stages of growth inferred in the previous paragraph.

[1] M. J. Edwards, P. K. Patel, J. D. Lindl, L. J. Atherton, S. H. Glenzer, S. W. Haan, J. D. Kilkenny, O. L. Landen, E. I. Moses, A. Nikroo, R. Petrasso, T. C. Sangster, P. T. Springer, S. Batha, R. Benedetti, L. Bernstein, R. Betti, D. L. Bleuel, T. R. Boehly, D. K. Bradley, J. A. Caggiano, D. A. Callahan, P. M. Celliers, C. J. Cerjan, K. C. Chen, D. S. Clark, G. W. Collins, E. L. Dewald, L. Divol, S. Dixit, T. Doeppner, D. H. Edgell, J. E. Fair, M. Farrell, R. J. Fortner, J. Frenje, M. G. Gatu Johnson, E. Giraldez, V. Y. Glebov, G. Grim, B. A. Hammel, A. V. Hamza, D. R. Harding, S. P. Hatchett, N. Hein, H. W. Herrmann, D. Hicks, D. E. Hinkel, M. Hoppe, W. W. Hsing, N. Izumi, B. Jacoby, O. S. Jones, D. Kalantar, R. Kauffman, J. L. Kline, J. P. Knauer, J. A. Koch, B. J. Kozioziemski, G. Kyrala, K. N. LaFortune, S. L. Pape, R. J. Leeper, R. Lerche, T. Ma, B. J. MacGowan, A. J. MacKinnon, A. Macphee, E. R. Mapoles, M. M. Marinak, M. Mauldin, P. W. McKenty, M. Meezan, P. A. Michel, J. Milovich, J. D. Moody, M. Moran, D. H. Munro, C. L. Olson, K. Opachich, A. E. Pak, T. Parham, H.-S. Park, J. E. Ralph, S. P. Regan, B. Remington, H. Rinderknecht, H. F. Robey, M. Rosen, S. Ross, J. D. Salmonson, J. Sater, D. H. Schneider, F. H. Sguin, S. M. Sepke, D. A. Shaughnessy, V. A. Smalyuk, B. K. Spears, C. Stoeckl, W. Stoeffl, L. Suter, C. A. Thomas, R. Tommasini, R. P. Town, S. V. Weber, P. J. Wegner, K. Widman, M. Wilke, D. C. Wilson, C. B. Yeamans, and A. Zylstra, Physics of Plasmas **20**, 070501 (2013).

[2] T. Dittrich, O. Hurricane, D. Callahan, E. Dewald, T. Döppner, D. Hinkel, L. Berzak Hopkins, S. Le Pape, T. Ma, J. Milovich, J. Moreno, P. Patel, H.-S. Park, B. Remington, J. Salmonson, and J. Kline, Phys. Rev. Lett. **112**, 055002 (2014).

[3] H.-S. Park, O. Hurricane, D. Callahan, D. Casey, E. Dewald, T. Dittrich, T. Döppner, D. Hinkel, L. B. Hopkins, S. Le Pape, et al., Physical Review Letters **112**, 055001 (2014).

[4] L. Rayleigh, *Scientific Papers II* (Cambridge, England, 1900).

[5] G. Taylor, Proceedings of the Royal Society of London. Series A. Mathematical and Physical Sciences **201**, 192 (1950).

[6] D. H. Sharp, Physica D: Nonlinear Phenomena **12**, 3 (1984).

[7] R. D. Richtmyer, Communications on Pure and Applied Math-

ematics **13**, 297 (1960).
[8] E. Meshkov, Fluid Dynamics **4**, 101 (1969).
[9] M. Brouillette, Annual Review of Fluid Mechanics **34**, 445 (2002).
[10] J. D. Lindl, *Inertial confinement fusion: the quest for ignition and energy gain using indirect drive*, vol. 2998 (Springer New York, 1998).
[11] J. D. Lindl, P. Amendt, R. L. Berger, S. G. Glendinning, S. H. Glenzer, S. W. Haan, R. L. Kauffman, O. L. Landen, and L. J. Suter, Physics of Plasmas **11**, 339 (2004).
[12] S. Atzeni and J. Meyer-ter Vehn, *The Physics of Inertial Fusion*, International series of monographs on physics (Oxford University Press, 2004).
[13] E. Moses, Plasma Science, IEEE Transactions on **38**, 684 (2010).
[14] S. P. Regan, R. Epstein, B. A. Hammel, L. J. Suter, H. A. Scott, M. A. Barrios, D. K. Bradley, D. A. Callahan, C. Cerjan, G. W. Collins, S. N. Dixit, T. Döppner, M. J. Edwards, D. R. Farley, K. B. Fournier, S. Glenn, S. H. Glenzer, I. E. Golovkin, S. W. Haan, A. Hamza, D. G. Hicks, N. Izumi, O. S. Jones, J. D. Kilkenny, J. L. Kline, G. A. Kyrala, O. L. Landen, T. Ma, J. J. MacFarlane, A. J. MacKinnon, R. C. Mancini, R. L. McCrory, N. B. Meezan, D. D. Meyerhofer, A. Nikroo, H.-S. Park, J. Ralph, B. A. Remington, T. C. Sangster, V. A. Smalyuk, P. T. Springer, and R. P. J. Town, Phys. Rev. Lett. **111**, 045001 (2013).
[15] T. Ma, P. K. Patel, N. Izumi, P. T. Springer, M. H. Key, L. J. Atherton, L. R. Benedetti, D. K. Bradley, D. A. Callahan, P. M. Celliers, C. J. Cerjan, D. S. Clark, E. L. Dewald, S. N. Dixit, T. Döppner, D. H. Edgell, R. Epstein, S. Glenn, G. Grim, S. W. Haan, B. A. Hammel, D. Hicks, W. W. Hsing, O. S. Jones, S. F. Khan, J. D. Kilkenny, J. L. Kline, G. A. Kyrala, O. L. Landen, S. Le Pape, B. J. MacGowan, A. J. Mackinnon, A. G. MacPhee, N. B. Meezan, J. D. Moody, A. Pak, T. Parham, H.-S. Park, J. E. Ralph, S. P. Regan, B. A. Remington, H. F. Robey, J. S. Ross, B. K. Spears, V. Smalyuk, L. J. Suter, R. Tommasini, R. P. Town, S. V. Weber, J. D. Lindl, M. J. Edwards, S. H. Glenzer, and E. I. Moses, Phys. Rev. Lett. **111**, 085004 (2013).
[16] We note that high fuel–ablator mix was seen in many, but not all, of the NIC implosions.
[17] S. W. Haan, J. D. Lindl, D. A. Callahan, D. S. Clark, J. D. Salmonson, B. A. Hammel, L. J. Atherton, R. C. Cook, M. J. Edwards, S. Glenzer, A. V. Hamza, S. P. Hatchett, M. C. Herrmann, D. E. Hinkel, D. D. Ho, H. Huang, O. S. Jones, J. Kline, G. Kyrala, O. L. Landen, B. J. MacGowan, M. M. Marinak, D. D. Meyerhofer, J. L. Milovich, K. A. Moreno, E. I. Moses, D. H. Munro, A. Nikroo, R. E. Olson, K. Peterson, S. M. Pollaine, J. E. Ralph, H. F. Robey, B. K. Spears, P. T. Springer, L. J. Suter, C. A. Thomas, R. P. Town, R. Vesey, S. V. Weber, H. L. Wilkens, and D. C. Wilson, Physics of Plasmas **18**, 051001 (2011).
[18] D. S. Clark, D. E. Hinkel, D. C. Eder, O. S. Jones, S. W. Haan, B. A. Hammel, M. M. Marinak, J. L. Milovich, H. F. Robey, L. J. Suter, and R. P. J. Town, Physics of Plasmas **20**, 056318 (2013).
[19] D. Clark, D. Hinkel, D. Eder, O. Jones, S. Haan, B. Hammel, M. Marinak, J. Milovich, H. Robey, J. Salmonson, et al., Bulletin of the American Physical Society **58** (2013).
[20] J. Rygg, O. Jones, J. Field, M. Barrios, L. Benedetti, G. Collins, D. Eder, M. Edwards, J. Kline, J. Kroll, O. Landen, T. Ma, A. Pak, J. Peterson, K. Raman, R. Town, and D. Bradley, Phys. Rev. Lett. **112**, 195001 (2014).
[21] S. Nagel, J. Rygg, L. Benedetti, T. Ma, M. Barrios, S. Haan, B. Hammel, T. Doeppner, A. Pak, R. Tommasini, et al., Bulletin of the American Physical Society **58** (2013).
[22] H. F. Robey, P. M. Celliers, J. D. Moody, J. Sater, T. Parham, B. Kozioziemski, R. Dylla-Spears, J. S. Ross, S. LePape, J. E. Ralph, M. Hohenberger, E. L. Dewald, L. Berzak Hopkins, J. J. Kroll, B. E. Yoxall, A. V. Hamza, T. R. Boehly, A. Nikroo, O. L. Landen, and M. J. Edwards, Physics of Plasmas **21**, 022703 (2014).
[23] B. A. Remington, S. W. Haan, S. G. Glendinning, J. D. Kilkenny, D. H. Munro, and R. J. Wallace, Phys. Rev. Lett. **67**, 3259 (1991).
[24] B. A. Remington, S. W. Haan, S. G. Glendinning, J. D. Kilkenny, D. H. Munro, and R. J. Wallace, Physics of Fluids B: Plasma Physics (1989-1993) **4**, 967 (1992).
[25] S. V. Weber, B. A. Remington, S. W. Haan, B. G. Wilson, and J. K. Nash, Physics of Plasmas **1**, 3652 (1994).
[26] B. A. Remington, S. V. Weber, M. M. Marinak, S. W. Haan, J. D. Kilkenny, R. J. Wallace, and G. Dimonte, Physics of Plasmas **2**, 241 (1995).
[27] M. M. Marinak, B. A. Remington, S. V. Weber, R. E. Tipton, S. W. Haan, K. S. Budil, O. L. Landen, J. D. Kilkenny, and R. Wallace, Phys. Rev. Lett. **75**, 3677 (1995).
[28] M. M. Marinak, S. G. Glendinning, R. J. Wallace, B. A. Remington, K. S. Budil, S. W. Haan, R. E. Tipton, and J. D. Kilkenny, Phys. Rev. Lett. **80**, 4426 (1998).
[29] C. Cherfils, S. Glendinning, D. Galmiche, B. Remington, A. Richard, S. Haan, R. Wallace, N. Dague, and D. Kalantar, Physical Review Letters **83**, 5507 (1999).
[30] S. Glendinning, J. Colvin, S. Haan, D. Kalantar, O. Landen, M. Marinak, B. Remington, R. Wallace, C. Cherfils, N. Dague, et al., Physics of Plasmas **7**, 2033 (2000).
[31] H. Robey, T. Boehly, P. Celliers, J. Eggert, D. Hicks, R. Smith, R. Collins, M. Bowers, K. Krauter, P. Datte, et al., Physics of Plasmas **19**, 042706 (2012).
[32] G. Kyrala, S. Dixit, S. Glenzer, D. Kalantar, D. Bradley, N. Izumi, N. Meezan, O. Landen, D. Callahan, S. Weber, et al., Review of Scientific Instruments **81**, 10E316 (2010).
[33] M. S. Plesset, Journal of Applied Physics **25**, 96 (1954).
[34] R. Epstein, Physics of Plasmas (1994-present) **11**, 5114 (2004).
[35] M. J. Edwards, J. D. Lindl, B. K. Spears, S. V. Weber, L. J. Atherton, D. L. Bleuel, D. K. Bradley, D. A. Callahan, C. J. Cerjan, D. Clark, G. W. Collins, J. E. Fair, R. J. Fortner, S. H. Glenzer, S. W. Haan, B. A. Hammel, A. V. Hamza, S. P. Hatchett, N. Izumi, B. Jacoby, O. S. Jones, J. A. Koch, B. J. Kozioziemski, O. L. Landen, R. Lerche, B. J. MacGowan, A. J. MacKinnon, E. R. Mapoles, M. M. Marinak, M. Moran, E. I. Moses, D. H. Munro, D. H. Schneider, S. M. Sepke, D. A. Shaughnessy, P. T. Springer, R. Tommasini, L. Bernstein, W. Stoeffl, R. Betti, T. R. Boehly, T. C. Sangster, V. Y. Glebov, P. W. McKenty, S. P. Regan, D. H. Edgell, J. P. Knauer, C. Stoeckl, D. R. Harding, S. Batha, G. Grim, H. W. Herrmann, G. Kyrala, M. Wilke, D. C. Wilson, J. Frenje, R. Petrasso, K. Moreno, H. Huang, K. C. Chen, E. Giraldez, J. D. Kilkenny, M. Mauldin, N. Hein, M. Hoppe, A. Nikroo, and R. J. Leeper, Physics of Plasmas **18**, 051003 (2011).
[36] We have run simulations with the cone up to 150 μm capsule radius, $CR \sim 7$.
[37] V. A. Smalyuk, M. Barrios, J. A. Caggiano, D. T. Casey, C. J. Cerjan, D. S. Clark, M. J. Edwards, J. A. Frenje, M. Gatu-Johnson, V. Y. Glebov, G. Grim, S. W. Haan, B. A. Hammel, A. Hamza, D. E. Hoover, W. W. Hsing, O. Hurricane, J. D. Kilkenny, J. L. Kline, J. P. Knauer, J. Kroll, O. L. Landen, J. D. Lindl, T. Ma, J. M. McNaney, M. Mintz, A. Moore, A. Nikroo,

T. Parham, J. L. Peterson, R. Petrasso, L. Pickworth, J. E. Pino, K. Raman, S. P. Regan, B. A. Remington, H. F. Robey, D. P. Rowley, D. B. Sayre, R. E. Tipton, S. V. Weber, K. Widmann, D. C. Wilson, and C. B. Yeamans, Physics of Plasmas (1994-present) **21**, 056301 (2014).

[38] V. Smalyuk, L. Atherton, L. Benedetti, R. Bionta, D. Bleuel, E. Bond, D. Bradley, J. Caggiano, D. Callahan, D. Casey, et al., Physical Review Letters **111**, 215001 (2013).

[39] O. Hurricane, D. Callahan, D. Casey, P. Celliers, C. Cerjan, E. Dewald, T. Dittrich, T. Döppner, D. Hinkel, L. B. Hopkins, et al., Nature (2014).

[40] V. Smalyuk, D. Casey, D. Clark, M. Edwards, S. Haan, A. Hamza, D. Hoover, W. Hsing, O. Hurricane, J. Kilkenny, J. Kroll, O. Landen, A. Moore, A. Nikroo, L. Peterson, K. Raman, B. Remington, H. Robey, S. Weber, and K. Widmann, Phys. Rev. Lett. **112**, 185003 (2014).

[41] D. T. Casey, Physical Review E accepted (2014).

[42] V. A. Smalyuk and S. V. Weber, in preparation (2014).

[43] S. Haan, L. Berzak Hopkins, D. Clark, D. Eder, B. Hammel, A. Hamza, D. Ho, O. Jones, A. Kritcher, K. LaFortune, et al., Bulletin of the American Physical Society **58** (2013).

[44] S. W. Haan and V. A. Smalyuk, in preparation (2014).

[45] J. L. Peterson, in preparation (2014).

[46] M. E. Cuneo, R. A. Vesey, D. B. Sinars, G. R. Bennett, I. C. Smith, B. W. Atherton, J. L. Porter, and D. F. Wenger, Plasma Science, IEEE Transactions on **39**, 2412 (2011).

[47] V. Smalyuk, S. Hu, J. Hager, J. Delettrez, D. Meyerhofer, T. Sangster, and D. Shvarts, Physical Review Letters **103**, 105001 (2009).

[48] N. E. Lanier, C. W. Barnes, S. H. Batha, R. D. Day, G. R. Magelssen, J. M. Scott, A. M. Dunne, K. W. Parker, and S. D. Rothman, Physics of Plasmas (1994-present) **10**, 1816 (2003).

[49] J. Fincke, N. Lanier, S. Batha, R. Hueckstaedt, G. Magelssen, S. Rothman, K. Parker, and C. Horsfield, Laser and Particle Beams **23**, 21 (2005), ISSN 1469-803X.

[50] W. W. Hsing and N. M. Hoffman, Phys. Rev. Lett. **78**, 3876 (1997).

[51] R. Reinovsky, W. Anderson, and W. Atchison, IEEE TRANSACTIONS ON PLASMA SCIENCE (2002).

[52] D. B. Sinars, S. A. Slutz, M. C. Herrmann, R. D. McBride, M. E. Cuneo, K. J. Peterson, R. A. Vesey, C. Nakhleh, B. E. Blue, and K. Killebrew, Physical Review Letters **105**, 185001 (2010).

[53] D. B. Sinars, S. A. Slutz, M. C. Herrmann, R. D. McBride, M. E. Cuneo, C. A. Jennings, J. P. Chittenden, A. L. Velikovich, K. J. Peterson, R. A. Vesey, C. Nakhleh, E. M. Waisman, B. E. Blue, K. Killebrew, D. Schroen, K. Tomlinson, A. D. Edens, M. R. Lopez, I. C. Smith, J. Shores, V. Bigman, G. R. Bennett, B. W. Atherton, M. Savage, W. A. Stygar, G. T. Leifeste, and J. L. Porter, Physics of Plasmas **18**, 056301 (2011).

[54] K. J. Peterson, D. B. Sinars, E. P. Yu, M. C. Herrmann, M. E. Cuneo, S. A. Slutz, I. C. Smith, B. W. Atherton, M. D. Knudson, and C. Nakhleh, Physics of Plasmas **19**, 092701 (2012).

[55] K. J. Peterson, T. J. Awe, E. P. Yu, D. B. Sinars, E. S. Field, M. E. Cuneo, M. C. Herrmann, M. Savage, D. Schroen, K. Tomlinson, and C. Nakhleh, Phys. Rev. Lett. **112**, 135002 (2014).

[56] J. D. Kilkenny, S. G. Glendinning, S. W. Haan, B. A. Hammel, J. D. Lindl, D. Munro, B. A. Remington, S. V. Weber, J. P. Knauer, and C. P. Verdon, Physics of Plasmas **1**, 1379 (1994).

[57] K. S. Budil, B. A. Remington, T. A. Peyser, K. O. Mikaelian, P. L. Miller, N. C. Woolsey, W. M. Wood-Vasey, and A. M. Rubenchik, Phys. Rev. Lett. **76**, 4536 (1996).

[58] S. G. Glendinning, S. N. Dixit, B. A. Hammel, D. H. Kalantar, M. H. Key, J. D. Kilkenny, J. P. Knauer, D. M. Pennington, B. A. Remington, R. J. Wallace, and S. V. Weber, Phys. Rev. Lett. **78**, 3318 (1997).

[59] C. J. Pawley, S. E. Bodner, J. P. Dahlburg, S. P. Obenschain, A. J. Schmitt, J. D. Sethian, C. A. Sullivan, J. H. Gardner, Y. Aglitskiy, Y. Chan, and T. Lehecka, Physics of Plasmas **6**, 565 (1999).

[60] J. P. Knauer, R. Betti, D. K. Bradley, T. R. Boehly, T. J. B. Collins, V. N. Goncharov, P. W. McKenty, D. D. Meyerhofer, V. A. Smalyuk, C. P. Verdon, S. G. Glendinning, D. H. Kalantar, and R. G. Watt, Physics of Plasmas **7**, 338 (2000).

[61] Y. Aglitskiy, M. Karasik, A. L. Velikovich, N. Metzler, S. T. Zalesak, A. J. Schmitt, J. H. Gardner, V. Serlin, J. Weaver, and S. P. Obenschain, Physica Scripta **2008**, 014021 (2008).

[62] A. Casner, D. Galmiche, G. Huser, J.-P. Jadaud, S. Liberatore, and M. Vandenboomgaerde, Physics of Plasmas **16**, 092701 (2009).

[63] L. Masse, A. Casner, D. Galmiche, G. Huser, S. Liberatore, and M. Theobald, Phys. Rev. E **83**, 055401 (2011).

[64] G. Huser, A. Casner, L. Masse, S. Liberatore, D. Galmiche, L. Jacquet, and M. Theobald, Physics of Plasmas **18**, 012706 (2011).

[65] J. Grun, M. H. Emery, C. K. Manka, T. N. Lee, E. A. Mclean, A. Mostovych, J. Stamper, S. Bodner, S. P. Obenschain, and B. H. Ripin, Phys. Rev. Lett. **58**, 2672 (1987).

[66] R. Taylor, J. Dahlburg, A. Iwase, J. Gardner, D. Fyfe, and O. Willi, Physical Review Letters **76**, 1643 (1996).

[67] K. Shigemori, H. Azechi, M. Nakai, M. Honda, K. Meguro, N. Miyanaga, H. Takabe, and K. Mima, Phys. Rev. Lett. **78**, 250 (1997).

[68] H. Azechi, M. Nakai, K. Shigemori, N. Miyanaga, H. Shiraga, H. Nishimura, M. Honda, R. Ishizaki, J. G. Wouchuk, H. Takabe, K. Nishihara, K. Mima, A. Nishiguchi, and T. Endo, Physics of Plasmas **4**, 4079 (1997).

[69] D. H. Kalantar, M. H. Key, L. B. Da Silva, S. G. Glendinning, B. A. Remington, J. E. Rothenberg, F. Weber, S. V. Weber, E. Wolfrum, N. S. Kim, D. Neely, J. Zhang, J. S. Wark, A. Demir, J. Lin, R. Smith, G. J. Tallents, C. L. S. Lewis, A. MacPhee, J. Warwick, and J. P. Knauer, Physics of Plasmas **4**, 1985 (1997).

[70] V. Smalyuk, O. Sadot, J. Delettrez, D. Meyerhofer, S. Regan, and T. Sangster, Physical Review Letters **95**, 215001 (2005).

[71] B. A. Remington, R. P. Drake, and D. D. Ryutov, Rev. Mod. Phys. **78**, 755 (2006).

[72] R. P. Drake, *High-energy-density physics: fundamentals, inertial fusion, and experimental astrophysics* (Springer, 2006).

[73] M. Marinak, G. Kerbel, N. Gentile, O. Jones, D. Munro, S. Pollaine, T. Dittrich, and S. Haan, Physics of Plasmas **8**, 2275 (2001).

[74] R. M. Darlington, T. L. McAbee, and G. Rodrigue, Comp. Phys. Comm. **135**, 58 (2001).

[75] O. Jones, C. Cerjan, M. Marinak, J. Milovich, H. Robey, P. Springer, L. Benedetti, D. Bleuel, E. Bond, D. Bradley, et al., Physics of Plasmas **19**, 056315 (2012).

[76] W. L. Kruer, in *Laser-Plasma Interactions and Applications* (Springer, 2013), pp. 221–242.

[77] P. Michel, S. Glenzer, L. Divol, D. Bradley, D. Callahan, S. Dixit, S. Glenn, D. Hinkel, R. Kirkwood, J. Kline, et al., Physics of Plasmas **17**, 056305 (2010).

[78] D. H. Munro, P. M. Celliers, G. W. Collins, D. M. Gold, L. B. Da Silva, S. W. Haan, R. C. Cauble, B. A. Hammel, and W. W. Hsing, Physics of Plasmas **8**, 2245 (2001).

[79] D. Hicks, B. Spears, D. Braun, R. Olson, C. Sorce, P. Celliers,

G. Collins, and O. Landen, Physics of Plasmas **17**, 102703 (2010).
[80] S. MacLaren, M. Schneider, K. Widmann, J. Hammer, E. Yoxall, B., J. Moody, M. Bell, P., L. Benedetti, D. Bradley, M. Edwards, T. Guymer, D. Hinkel, W. Hsing, M. Kervin, N. Meezan, A. Moore, and J. Ralph, Phys. Rev. Lett. **112**, 105003 (2014).
[81] These (unpublished) modeling studies by N. Meezan et. al. suggest this higher sensitivity in the picket is roughly the same for the low–foot and high–foot pulses, and is believed to be related to processes which occur before the laser spot reaches the hohlraum wall, such as ablation of the plastic window covering the hohlraum laser entrance hole (LEH). The basic correctness of this prescription has been empirically verified by one of us (H. F. Robey) through extensive post–shot modeling studies of VISAR targets.
[82] S. W. Haan, Physical Review A **39**, 5812 (1989).
[83] S. W. Haan, Physics of Fluids B: Plasma Physics **3**, 2349 (1991).
[84] B. L. Henke, E. M. Gullikson, and J. C. Davis, Atomic data and nuclear data tables **54**, 181 (1993).
[85] G. Kyrala, J. Kline, S. Dixit, S. Glenzer, D. Kalantar, D. Bradley, N. Izumi, N. Meezan, O. Landen, D. Callahan, et al., Physics of Plasmas **18**, 056307 (2011).
[86] N. Meezan, L. Atherton, D. Callahan, E. Dewald, S. Dixit, E. Dzenitis, M. Edwards, C. Haynam, D. Hinkel, O. Jones, et al., Physics of plasmas **17**, 056304 (2010).
[87] Shock timing experiments without liquid deuterium have been recently fielded using the same coating strategy to protect from M–band radiation, discussed below. See Ref. 103.
[88] The idea is that optical depths much greater than 2 are equally opaque to the detector. For example, if the average OD is 1.5, we design the perturbation so that the amplitude of the first harmonic at the experiment time is less than 0.5.
[89] A typical outer surface roughness profile is shown in Fig. 3 of Ref. 18. The measured power spectral density of a typical target at mode 60 is around 0.3 nm^2, corresponding to a characteristic amplitude $\sqrt{4\pi(0.3)} \sim 2$ nm. The ignition specification for the mode 60 power is 1 nm^2, for an amplitude of about 3.5 nm. The amplitude (OD) versus time for these initial values may be inferred from Fig. 10 by simply scaling the amplitude of the (3/64) μm curve, which is in the linear regime at 21 ns. For example, if an initial amplitude of (3/64)μm $\approx$ 47 nm reaches an amplitude (OD) of 0.1 at 21 ns, the amplitude of a 3 nm initial perturbation will have grown to (0.1)(3)/(47) $\approx$ 0.006, which is below the noise value of 0.01. Also, extrapolating the curves, one can infer that the 3 nm perturbation will be linear for most of the acceleration, even allowing for considerable uncertainty in the growth factor. For instance, even if the growth factor is off by a factor of 15, so that the 3 nm growth is actually represented by the 47 nm calculation, the curves indicate the growth will still be linear until just before peak velocity at 22 ns.
[90] R. Betti, V. N. Goncharov, R. L. McCrory, P. Sorotokin, and C. P. Verdon, Physics of Plasmas **3**, 2122 (1996).
[91] S. W. Haan (2013), private communication.
[92] R. M. More, K. H. Warren, D. A. Young, and G. B. Zimmerman, Physics of Fluids (1958-1988) **31**, 3059 (1988).
[93] D. A. Young and E. M. Corey, Journal of Applied Physics **78**, 3748 (1995).
[94] M. A. Barrios, T. R. Boehly, D. G. Hicks, D. E. Fratanduono, J. H. Eggert, G. W. Collins, and D. D. Meyerhofer, Journal of Applied Physics **111**, 093515 (2012).
[95] P. Sterne (2013), private communication.
[96] O. S. Jones (2013), private communication.
[97] In this example, we simply generate the density profile by simulating a 2xSi capsule, which we then post–process for the different ablator cases. However, in order to actually generate the same density profile with different layered ablators, the drives would need to be different.
[98] B. Hammel, S. Haan, D. Clark, M. Edwards, S. Langer, M. Marinak, M. Patel, J. Salmonson, and H. Scott, High Energy Density Physics **6**, 171 (2010).
[99] E. Loomis, D. Braun, S. Batha, and O. Landen, Physics of Plasmas **19**, 122703 (2012).
[100] J. Peterson, D. Clark, L. Suter, and L. Masse, Bulletin of the American Physical Society **58** (2013).
[101] We have been unable, so far, to force either mode 60 or 90 to invert in low–foot simulations by simply modifying the simulation in physically reasonable ways. This may be related to our measurement that shows the modes actually do grow positively (see Fig. 14c). Following a suggestion by R. Tipton, we are able to force inversion by dropping a number of terms in the radiation diffusion equations, which does not have any physical justification, but is a different way of generating radiographs of inverting scenarios. We have tested the analysis procedure against the radiographs produced from such simulations, as well as simulations using different mode numbers that actually are predicted to invert, in addition to what is discussed in the text.
[102] Because, in this example, the wavelengths of modes 60, λ_{60} and 90, λ_{90}, are related by $\lambda_{60} = (3/2)\lambda_{90}$, the *distance* between markers in Fig. 25 is also consistent with two wavelengths of mode 90, which would imply both modes have grown positively and that the mode 60 marker line is the connection joint. However, this possibility is ruled out if in addition to just the distance between markers, we also examine the spike pattern in between.
[103] H. F. Robey, J. D. Moody, P. M. Celliers, J. S. Ross, J. Ralph, S. Le Pape, L. Berzak Hopkins, T. Parham, J. Sater, E. R. Mapoles, D. M. Holunga, C. F. Walters, B. J. Haid, B. J. Kozioziemski, R. J. Dylla-Spears, K. G. Krauter, G. Frieders, G. Ross, M. W. Bowers, D. J. Strozzi, B. E. Yoxall, A. V. Hamza, B. Dzenitis, S. D. Bhandarkar, B. Young, B. M. Van Wonterghem, L. J. Atherton, O. L. Landen, M. J. Edwards, and T. R. Boehly, Phys. Rev. Lett. **111**, 065003 (2013).